Optimization of specimen geometries for mechanical tests: Setting the standard for tissue preparation

A Thesis

SUBMITTED TO THE FACULTY OF

UNIVERSITY OF MINNESOTA

BY

Fluvio Luis Lobo Fenoglietto

IN PARTIAL FULFILLMENT OF THE REQUIREMENTS

FOR THE DEGREE OF

MASTER OF SCIENCE

Victor H. Barocas

August 2015

Abstract

Mechanical tests have been used in industry and academia for the characterization of ceramics, metals, polymers, and biological tissues. While standard testing protocols have been established for manufacturable materials, only adaptations of these procedures exists for biologics. Simulation studies have been conducted to show the performance of these adaptations, focusing on the effect of boundary conditions and the homogeneity in loading distribution. However, these studies have not been used to optimize controllable variables such as the specimen geometry, cutting mechanisms, and gripping methodologies, with the goal of improving experimental outcomes. Moreover, previous studies have not include structural material models that may represent the microstructure of biological tissues more accurately. Using a novel Finite Element Analysis (FEA) platform for biomechanics, our goal is to optimize the geometry of inhomogeneous soft tissue samples, even stress distribution and avoid early material failure at intensities.

Table of Contents

List of Tables

List of Figures

The Human Tissue Properties Database

The Center for Research in Education and Simulation Technologies (CREST) can be best described as a research and development group that spun-off SimPORTAL, a simulation training program for procedurally oriented departments within University of Minnesota's Medical School. Within the medical school, CREST led the development of novel curricula and simulators to support the education of healthcare professionals. Virtual reality and physical simulators are used to train medical school residents, physicians, army medics, and other healthcare professionals. However, commercially available simulators lack anatomical and material realism. The simulators developed at CREST are known for their realism. The main objective of CREST is to increase fidelity through the implementation of materials that react as human tissues, without compromising the anatomical accuracy of the models. In order to achieve this goal, CREST currently leads the Human Tissue Properties Database (HTPD) program. The overarching goal of the HTPD project is to determine the optical, electrical, mechanical, and thermal properties of all human tissues. The breadth of this objective requires the establishment of a systematic, repeatable, and expandable protocol that allows for the long-term acquisition of physical tissue data. With time, the project also seeks to improve old or establish new protocols that will increase the accuracy and repeatability of the data. Effectively creating a resource for internal development at CREST, for academic institutions, the industry, and the government. The HTPD project currently receives support from the Army Research Labs (ARL) in Orlando, FL.

The mechanical properties of biological tissues

The mechanical properties of human tissues have been observed before the existence a formal field of biomechanics [1]. However, one could argue the field consolidated between the early 1960s and late 1990s with the work of scientists like Y. C. Fung, J. D. Y. Lanir, O. Immanuel, Humphrey, and F. C. P. Yin, just to name a few [2, 3, 4, 5, 6]. Their combined efforts are the foundations of modern biomechanics, tissue mechanics, and arguably computational biomechanics. These scientists, biomechanicians or tissue mechanicians, adapted uniaxial and biaxial mechanical testing protocols for the characterization of biological tissues [1, 7]. Their tests lead to the observation of the non-linear, viscoelastic, and anisotropic mechanical behavior of biological tissues. These discoveries motivated the development of testing protocols and analysis methodologies that could characterize the complexity of the material response [8]. In spite of the consensus regarding testing procedures, the process of tissue sample preparation has yet to see some standardization.

Regardless of their widespread implementation, the sample preparation section of these protocols has not been optimized for biological materials. For uniaxial experiments, researchers have had to design alternatives to the standard dog bone or dumbbell specimen. This has been the solution to the existence of a single standard outlining the dimensions of this specimen [9]. With examples of specimens ranging between 30 mm – 100 mm in length [9], this standard cannot be considered as a template for the dissection of biological samples. Furthermore, the standard does not provide any indications of relationships between specimen dimensions, which could be used for the re-design and adaptation of the

dog bone or dumbbell shape. Consequently, researchers have had to deal with variability that can be rooted to inefficient specimen design.

Fewer standardization exists in biaxial experiments, where the field has been split into the classical square and the cruciform specimens. In addition to a detailed description of the testing protocols for biaxial testing, Y. C. Fung depicts a square specimen connected to the two (2) axis of the system via hooks and strings [1]. Researchers such as Lanir and Humphrey also used the square specimen for biaxial testing [2, 6]. Even today, prominent tissue mechanics lab also use square specimens and hooks for the majority of their biaxial tests [8, 10]. Hooks are advantageous but also cumbersome. Hooks are assumed to act as point-loads on the sample, thus allowing for an unconstrained biaxial deformation of the sample [10]. Conversely, the placement of hooks must be meticulous, especially in the absence of pivoting mechanisms that may correct misalignment. Moreover, the piercing of tissue samples represents a biohazard to the operator, particularly when samples are human cadaveric. In light of these issues, the cruciform specimen has been the preferred solution for multiple researchers [10]. Cruciform specimens eliminate the need for hooks, but let results succumb to the constrained deformations imposed by straight grips. Sacks and Sun studied the differences between cruciform and square specimens, including the boundary conditions imposed by their corresponding technique [10]. Sacks and Sun determined that, “although not ideal,” square specimens and hooks generated greater stresses within the sample [10]. Without seeking to refute these results, it is important to understand that certain variables were considered throughout their experiments. First and foremost, only one cruciform design was compared to the square specimen. The tested design, featuring four (4) sharp angles, was not modified in order to reduce predictable stress concentrations.

In addition, the square sample was simulated using point-loads as hooks. This assumption neglects the intensities that should arise from the uneven interface between the hooks and the tissue.

The optimization of the design of any testing specimen is challenged by the availability of the material. Biological tissues, specifically human samples, are not readily available for research. To obtain human tissue samples, research groups have to seek consent and screen for contagious diseases. Moreover, some tissue specimens are also small in nature, which translates to fewer experiments per cadaver. As a result of these obstacles, computational methods such as Finite Element Analysis (FEA) represent an attractive and effective alternative toward solving the problem. Sacks and Sun focused their comparison between square and cruciform experiments using FEA. This approach enabled them to simulate several experiments while examining the effect of some variables (e.g. direction of deformation, number of hooks, etc.) on their results [10]. Sacks and Sun recognized the potential of FEA for similar applications and even their attempts were limited by the robustness of their in-house method [10]. Since then, several research groups have focused on the implementation of FEA for all aspects of tissue mechanics simulation. With the exponential growth in computational power, simulation has become a necessity within academia, industry, and government (e.g. regulatory agencies such as FDA). Within academia, the University of Utah can be highlighted for developing an open-source, non-linear, large-deformation FEA platform called FEBio [11]. FEBio's material library includes widely used constitutive models for hyperelastic materials (e.g. Neo-Hookean, Mooney-Rivlin, Ogden, etc.) and biological tissues (e.g. Fung Orthotropic, Arruda-Boyce, blah blah). In addition, FEBio has been formulated to handle the most characteristic

properties of biological tissues, such as viscoelasticity and incompressibility [11]. FEBio takes full advantage of the finite element method to deliver one of its most relevant feature, the ability to create structural models. In fact, some of the most prevalent structural models in the literature [12] have been replicated with FEBio to shown its flexibility. Through the implementation of FEBio, structural models have been able to replicate mechanical phenomena observed in tissues [13]. On the latest iteration of the FEBio suite, two- and three-dimensional continuous fiber distributions have been enabled to ensure model stability. Users can chose normal and Von-Mises distributions of fibers, in addition to specifying the orientation of these fibers, in order to effectively simulate anisotropic materials [11].

By leveraging the most novel biomechanics-specific FEA platform (FEBio), the following study was aimed towards improving the outcome of mechanical tests through the optimization of testing specimen designs. Variations of such testing specimens were evaluated using FEBio, in order to determine the geometric features that shifted stress concentrations from undesired to preferred regions of the sample.

Hypothesis

1. Geometric modifications of testing specimens, including the addition of features and the establishment of dimensional constraints and ratios, will enhance homogeneity in stress distribution and reduce stress concentrations that may lead to early material failure.
2. The implementation of an incompressible, mixture or composite solid material model, inspired from the micro-structure of biological tissues, may lead to further design modifications of testing specimens.

Objectives

1. Identify standard or most common specimen geometries used for uniaxial and biaxial mechanical-tensile testing

2. Assign dimensions and establish relations between features of each specimen geometry, with the goal of reducing the number of independent variables

3. Generate permutations of the specimen geometries by modifying independent design variables and ratios

4. Define an incompressible, mixture or composite material model for the Finite Element Analysis of all specimen geometries

Mechanical testing specimens

Sample dimensions are essential in most characterization protocols (mechanical, electrical, thermal and optical). In most cases, samples must cover a certain area or have a minimum thickness. Instead, in the case of mechanical characterization, samples must be prepared or dissected in a test-specific shape or geometry. These geometries have been designed to concentrate the deformation within a region of known dimensions. These dimensions are fundamental for the calculation of the strain, the stress, and the constitutive relation between the two.

Uniaxial tensile tests and the dog bone sample

Uniaxial tests are the most fundamental characterization tests in mechanics. As the name indicates, the uniaxial tensile tests entails the stretching of a sample along a single axis of orientation. In addition to exposing the elastic response of the material, these tests pursue the failure of the material in tension. In order to significantly concentrate stresses within the material, the dog bone or dumbbell shape has been designed for uniaxial tests (Figure 1). Derived from a rectangle, the transition from wider shoulders to a narrow neck allows for the deformation to move away from the gripped ends. The narrow cross-section of the neck, compare to that of the shoulder, generates higher stresses, thus increasing the probability of failure. The resultant design resembles the objects that give rise to the specimen's colloquial name.

The dog bone or dumbbell sample was defined using five (5) variables (Figure 1). These variables and the overall design of the specimen was derived from a rectangle of length l_o and width w_o, while a smaller rectangle of length l_i and width w_i outlined the neck region. The transition between w_o and w_i left four (4) rectangular corners where

stresses concentrate due to the abrupt change in cross-section area. Three-point arcs, defined by a radius R, were used to smooth this transition and avoid material failure at early strains. Finally, the gripping area of the specimen was described by w_o and l_g, where the latter was defined as a fraction of the difference between l_o and l_i. The list of variables describing the dog bone specimen has been compiled in Table 2. The relations between these variables, used to scale the dig bone design, were summarized in Table 3.

Biaxial planar tests, the classical square, and the cruciform

Biaxial tests were designed to characterize the mechanical properties of anisotropic materials. The properties of these materials are dependent to the orientation of the mechanical stimulation. Biological tissues are good examples of anisotropic materials. In a biaxial test, a material sample is stretched in orthogonal directions without reaching failure. Here, the objective of a biaxial experiment consists of concentrating the deformation at the center of the sample. Given the test configuration, the classical and most common geometry used as a testing specimen consists of a square. Although easy to prepare, the square shape becomes more of an issue when gripping. Y. C. Fung introduced the implementation of hooks as part of the testing set-up [1, 2, 3]. The complications that arise from the implementation of hook grips led to the development of the cruciform-shaped sample (Figure 2). With the desire of using more standard methods of gripping (e.g. straight clamps), the extensions or arms of the cruciform geometry eliminate the need for hooks. In spite of this advantage, concerns have been raised regarding the effect of the cruciform arms on the stress distribution. Within the field of biomechanics and tissue mechanics, a simulation study revealed considerable differences between the stresses at these locations [10]. However, no additional modifications were suggested nor made to the

cruciform designs. Modifications which could improve the distributions and support the use of cruciforms specimens.

The cruciform used in this study was defined by four (4) dimensional variables (Figure 2). The width between the ends of the cruciforms arms was described by w_o, while the width and the length of such arms were given by w_i and w_a respectively. The resulting corners were treated with three-point arches defined by a radius R. The list of variables describing the cruciform specimen has been compiled in Table 5: Cruciform dimensions. The relations between these variables, used to scale the dig bone design, were summarized in Table 6: Cruciform geometric relations*Table 3*.

Geometric variants

In order to optimize the current design of testing specimens, geometric variants were created for dog bone and cruciform specimens. For each variant, dimensions were modified on the basis of ratios, with the goal of reducing or eliminating undesired stress concentrations and early material failure. These ratios, also referred to as dimensional ratios, consisted of proportions between the dimensions used to outline or describe the original specimen.

Width and length ratios of the dog bone

As discussed previously, stress concentrates in regions were abrupt changes in cross-section area occur. To reduce such concentrations, right angles have been reduced with three-point arches and curves. Although these curves are an essential method toward the reduction of stress concentrations and early material failure, their effect was studied using the cruciform specimens. Instead, the dig bone specimens were used to study the

effect of the ratios between widths and lengths, which ultimately give rise to undesired concentrations. To study such effect, geometry variants of the dog bone specimen were designed on the basis of the dimensional ratios shown in Table 3. The dimensions of the resulting geometry variants were summarized in Table 4: Dog bone geometric variants.

Smoothing cruciform corners with arches or curves

Compared to the dog bone, the cruciform represented a much simpler model. The symmetry of the cruciform allowed for most of these variables to be defined as ratios of a single value. In fact, as summarized in Table 6, three (3) dimensions were defined given the outer width (w_o) of the cruciform. The cruciform model was used to study the effect curvatures as an alternative towards reducing stress concentrations. In the case of cruciforms, stress concentrates at the intersection between the cruciform arms. The alternative to these concentrations consists on the addition of three-point arches or curves defined by a radius R. An example of these arches or curves has been included in Figure 2. In order to study the effect of these arches, each geometric variant was characterized by a different radius of curvature R. The dimension of all resultant variants was summarized in **Error! Reference source not found.**.

The design process

Three dimensional (3D) solid models of geometric variants were designed using SOLIDWORKS 2014 (Dassault Systèmes Corp.). Every model was designed using the variables presented in Table 2 & Table 5 and the corresponding dimensions summarized in Table 4 & **Error! Reference source not found.**.

Specimen design optimization

Variations of the original testing geometries were evaluated using the Finite Element Method (FEM). Original specimens and design variations were subjected to their respective, displacement-controlled, tensile experiments. Boundary conditions were replicated to the capabilities of the implemented simulation suite. In addition to experimental parameters, a structural material model was chosen to simulate biological tissues. Finally, the resultant strain and stress distribution were further segmented along features that changed across design variants. This segmentation of the data allowed to provide a quantitative and localized means of evaluating the effectiveness of weakness of the geometric variants.

Geometry meshing

Although meshing could be completed within FEBio, the FEA platform of choice, its meshing capabilities fall short of dedicated algorithms like CUBIT. Developed in Sandia National Laboratories, CUBIT can be described as a "full-featured software toolkit for the robust generation of two- and three- dimensional finite element meshes" [14]. Design variants were imported into CUBIT for three-dimensional, hexahedral meshing. Mesh refinement parameters were similar but not equal across geometry variants. Most importantly, the quality of every mesh was assess using CUBITs inspection tools and parameters [14].

The material model

Rather than choosing a single constitutive equation to describe the mechanical behavior of biological tissues, a micro-structure inspired model was implemented. As discussed earlier, tissues are viscoelastic, incompressible materials with non-linear,

sometimes exponential, pseudo-elastic tensile mechanical behavior [1, 4, 5]. Aside from viscoelasticity, the selected structural model encompasses all of these tissue properties on each element of the model's mesh. Given the brief nature of the deformations simulated in this study, viscoelasticity (or time dependence) was excluded from the model. To account for the remaining properties, the model consisted of two independent components that simulate the histological structure of a majority of tissues. Each element of the model was composed of an incompressible, isotropic ground matrix enclosing fibers which, in tension, give rise to the anisotropic, exponential behavior observed in collagen fibers and collagenous tissues.

Structural models are assembled as "solid mixtures" in FEBio [11]. Solid mixtures consist of "stable" and "unstable" materials. Stable materials can compose an entire material independently, hence usually defined as the ground matrix or substance of structural models. On the other hand, unstable materials need to be modeled in conjunction with a ground matrix in which the former are embedded. Within FEBio, this concept of stability has been fabricated to simulate the dependence of fibers (e.g. elastin and collagen) to the viscous matrix of biological tissues [11]. In the simplest example, one may consider the buckling of fibers. Collagen, as well as other fibers, have been designed to sustain tension. Under compression, collagen fibers would buckle. However, since these fibers are suspended within a viscous matrix, the material that composes such matrix sustains the compression [11, 15]. In general, the mechanical behavior of the solid mixture consists of the combined responses of the stable and unstable components or, as referred to hereinafter, the ground matrix and fibers.

The ground matrix

Commonly used in the literature to model ground substances, the Mooney-Rivlin material was implemented for the structural model presented here [4, 5, 12, 13]. The constitutive formulation of the Mooney-Rivlin model (Equation 1) was simplified through the assignment of material isotropy and incompressibility (Equation 6-Equation 9). Finally, the kinematics corresponding to the mechanical experiment, uniaxial and biaxial, led to the derivation of the respective formulation for the mechanical response of the material (Equation 14 – uniaxial, Equation 21 – biaxial).

The fibers

To model the non-linear, exponential mechanical response attributed to fibers such as collagen, FEBio provides a variety of constitutive formulations [11]. These formulations share some similarities with equations used in early structural models [4, 5], allowing the user to specify the orientation of fibers in some instances. While some of these formulations in FEBio are specific to single fibers, the most stable models consist of continuous distributions [11]. Within this context, stability refers to volume fluctuations and warping of the mesh. Fiber distributions are not a novel concept [4], and still represent the most effective alternative towards simulating anisotropy of biological materials [13, 12]. Therefore, a continuous, two-dimensional, Von-Mises distribution of fibers with exponential, power-law mechanics was used for the present structural model [11]. The strain energy density function of the fibers, including the distribution components, are shown in Equation 32 & Equation 33.

The structural model

The strain energy function of the structural model resulted from the addition of the constitutive formulas for each component, ground matrix and fibers (Equation 34 & Equation 35). The final forms of the strain energy density function were derived on the basis of the experiment-specific kinematics (Equation 36 & Equation 37).

Validation of the material model

Thus far, only theoretical information has been given to justify the use of a micro-structure inspired model to simulate tissues. In the process, claims have been made regarding the properties of each model component (ground matrix and fibers). The following experiments have been designed to validate such claims and provide more insight on the structural model itself.

For simplicity, all of the experiments were performed on a unit-cube. The unit-cube was designed and meshed following the methodology described previously. Material properties, experimental boundary conditions, and FEA parameters were specified using PreView and FEBio 2.3. PostView was used for data visualization, while several MATLAB®-based scripts were developed to extract and process element data. These algorithms were specifically designed to identify, extract, and compute statistics (Mean, Standard Deviation, and Standard Error) on values of strain, stress, and volume corresponding to each element of the mesh.

Isotropic, incompressible ground matrix

The first component of the structural model, the ground matrix, has been said to consist of an isotropic, incompressible Mooney-Rivlin material. Theoretically, an isotropic material exhibits physical responses that are independent of the orientation of the stimulus.

In order to validate isotropy, a unit-cube model consisting of a Mooney-Rivlin material was suggested to an ideal uniaxial tensile experiment. The ideal experiment was simulated by allowing the sliding of surfaces adjacent to axes of symmetry, while constraining their movement along their plane normal (Figure 4). Material model constants, experimental and simulation parameters were summarized in Table 8. In this experiment, an isotropic material would deform equally in the plane perpendicular to the direction of tensile stimulus.

The uniaxial tensile experiment consisted of an applied displacement along X (1), as shown in Figure 6. The elongation in X (1) caused the shortening, or narrowing, of the material along the $Y - Z$ $(2 - 3)$ plane. In order to verify an equal shortening along the $Y - Z$ $(2 - 3)$, and thus isotropy, the Green-Lagrangian strain (E) along Y and Z was measured for every element of the model's mesh (Figure 6 & 7). When graphed simultaneously, the equivalence between Y and Z Green-Lagrange strains was evident (Figure 8). The measured strains were also equal to the predicted strains (Figure 8), which were calculated by directly equating the stretch ratios along the plane perpendicular to the direction of pull (Equation 6). Incompressibility of the ground matrix was validated by measuring the "relative volume" at every element of the material (Figure 9). The "relative volume," or the volume change, of every element remained at a value of one $(J = 1)$, following the incompressibility requirement (Equation 7). Using FEBio, incompressibility was ensured through penalty factors and Lagrangian multipliers [11]. Further validation of the ground matrix model came from the comparison between the measured and calculated stress-strain response of the material (Figure 10). Like in the case of the Y and Z Green-Lagrange strains,

the calculated stress response matched the values measured from the mesh elements (Figure 10).

Anisotropy of the model through embedded fibers

One of the main objectives of a structural model is to replicate anisotropy by simulating the components or structures which, physiologically, would give rise to orientation-dependent mechanical properties. As discussed previously, fiber families are responsible for the orientation dependence of the material's mechanical properties. Moreover, fibers give rise to the non-linear exponential mechanical behavior of biological tissues. The best example of this is collagen, the most common structural protein across biological tissues. Single collagen fibers have been tested using atomic force microscopy, among other techniques, to determine the non-linear mechanics of the fibers [16, 17].

In order to integrate fibers into the structural model, continuous fiber distributions were assigned through FEBio. A feature of the most recent iteration of FEBio, continuous distributions of fibers have been present in the literature since the inception of structural models [4]. More recent work has been focused towards understanding the influence of these distributions in three-dimensional models [12, 13]. FEBio allows the user to customize several properties of these distributions. In all the simulations pertaining to this study, two-dimensional Von Mises distributions of fibers were used to represent fibers aligned along the primary axis of deformation (Figure 15 & 16).

In order to validate the mechanical response of the Von Mises distribution, the unit cube approach was implemented once again. The results of the overall response are shown in Figure 14. In compressibility of the material was ensured and also validated (Figure 13).

FEA-based study

The design of geometric variants was evaluated using FEA and a technique named objective partitioning. The FEBio suite was used to simulate tensile experiments pertinent to each specimen and variant. The convoluted FEA data was further simplified and analyzed through objective partitioning. This technique was used to segment FEA results through standard volumes or partitions.

Simulated tensile experiments

Each specimen variant was subjected to its corresponding tensile experiment. Simulations were prepared using PreView, FEBio's FEA pre-processor. Dog bone variants were subjected to a displacement stimulus along a single direction (X). On the other hand, cruciform variants were subjected to simultaneous, displacement stimuli along orthogonal directions ($X - Y$). Experiment parameters were summarized in Table 9 for the uniaxial and Table 10 for the biaxial test. In an attempt to make simulations realistic, gripping boundary conditions were applied to the geometric variants by constraining transverse deformation on the surfaces being displaced. Similarly to the validation models, the symmetry boundary condition was applied to allow for surfaces to slide along planes while being constrained along the normal of such planes.

Simulation results were visualized using PostView, FEBio's FEA post-processor. Physical data of interest, including displacement, strain, stress, and relative volume, was exported from PostView as –ascii delimited files. Each file contained nodal coordinates, element connectivity, and element value data. This information became essential when segmenting the FEA results.

Objective partitioning

Altogether, the FEA results expanded over four (4) dimensions of data (x, y, z, and time). Yet, the data crucial to the study was localized. In order to extract data from specific sections of a volume, FEBio allowed for mesh partitioning prior to simulation. Although effective, the process was highly dependent on the size of the mesh elements. In order to partition the mesh without depending on its elements, the method of objective partitioning was developed. The name was based on the idea of implementing standard shapes (e.g. spheres, cylinders) to delimit regions of interest (ROIs) within the mesh. Given that these shapes were defined by variables independent to the mesh (e.g. radius, height), and the elements within such mesh, the process was held as objective.

Regions of interest (ROIs)

In spite of having collected data over the entire volume of each geometric variants, the data within regions of interest (ROIs) was used as the basis of the design evaluation. These ROIs consisted of sections of the variants where stresses were desired and undesired. Four (4) ROIs were defined across all geometries: target, intensities, maximum, and boundary conditions. Each region has been described in Table 11 and depicted in Figure 17 & 18. While the dimensions of the ROIs (their radius) remained constant among geometric variants, the origins depended on the dimensions of each variant.

Element centroids

Once the ROIs were created within the mesh, their bounds were used to delimit and select elements within their reach. Initially, elements having all composing nodes fall within the bounds of the ROI were selected. However, in many instances, only several of the nodes fell within the bounds of the ROI. In order to maximize the number of selected

elements, while reducing the number of computations, a single reference value was used. The centroid of the element, calculated from the coordinates of the element's nodes, was used as the single reference. The calculation of element centroids was performed by an algorithm built in MATLAB®.

Tracking deformation

The downfall of objective partitioning became evident with the deformation of the target mesh. By being independent to the target mesh, ROIs did not change position with the deformation of the target mesh. Provided with the challenge, two solutions were considered. The most straight-forward solution consisted on following the nearest element centroid or node, throughout the simulation. While this represented the least computationally expensive solution, the methodology could have made the process dependent to an element or node unrepresentative of the region. This could be particularly true at intensities. In order to avoid this issue, while preserving the core idea behind the solution, an alternative was developed on the basis of three-dimensional displacement fields. Rather than looking at the displacement of a single reference, the ROIs were used measure the average displacement within the delimited volume, and use the measurements to update the ROIs centroid position. In an iterative manner, an algorithm repeats the calculation until the change in centroid position, of the ROIs, fell below a tolerance. In order to update the position of the ROIs, or track the deformation, an MATLAB® algorithm was developed. The algorithm included visualization routines that allowed for quick measurement verification. Samples of these output graphs were shown in Figure 17 & 18, but an entire series has been compiled in Figure 19.

Evaluation ratios

The data segmented through ROIs was used to calculate ratios, a more meaningful quantity for the evaluation of geometric variants. In ideal mechanical experiments, uniaxial or biaxial, concentrations occur at σ_t. The ideal case assumes that a significant percentage of the input mechanical stimulus was transferred to the target, hence $\sigma_t \approx \sigma_{bc}$. However, in such ideal scenario no intensities would exist ($\sigma_{si} \approx 0$). Realistically, concentrations occur at intensities and gripped boundaries ($\sigma_{si}, \sigma_{bc} \gg \sigma_t$). Therefore, in order to evaluate design variants, ratios between concentrations were calculated and compared to the ideal case ($\frac{\sigma_t}{\sigma_{si}} \approx 1$). The previous statements also assumed that maximum stresses occur at the regions of expected concentrations σ_{si} or σ_{bc}. As listed in Table 11, an additional ROI corrects for the case where a maximum stress does not fall within the location of expected intensity σ_{si}. In general, the ratios used for the analysis of the geometric variants are: σ_t/σ_{si}, σ_t/σ_{max}, and σ_t/σ_{bc}.

Study results and analysis

Dog bone or dumbbell variants

The stress component of interest for the simulated uniaxial experiments was that parallel to (along) the direction of deformation (σ_{xx}). Effective dog bone or dumbbell samples are those in which the stress ratio between target and the boundary is greater than one ($\frac{\sigma_t}{\sigma_{bc}} > 1$). This is reasonable given the purposely-designed narrow neck region of the variants. Of course, this assumes that the stress intensity existing at the change in cross-section area (between the shoulders and the neck of the dog bone) has been reduced through curvatures and/or arcs. As discussed earlier, all cruciform variants used three-point arcs with the largest possible radius. This was done on purpose as the effect of the radius pertained more to the cruciform variants. Here, the maximum stress was used instead of the stress at the expected intensity (σ_{max}). In general, for simulation states 5, 10, 15, and 20, the target to maximum and boundary condition were plotted against the dimensional ratios defined for the dog bone geometry (α, β).

The results of the analysis were compiled between Figures 20 - 23. The results show that the most effective dog bone variants are those in which the ratio of the lengths (α) approaches one (1), while the ratio of the widths (β) approaches zero (0). However, in order to truly select an effective combination of the dimensional ratios, both graphs (Figure 20 & 21) must be examined carefully. In Figure 20, it is clear that an overall increase in the ratio of the target to the maximum stress can be achieved by increasing the ratio of the lengths (α). In other words, by designing dog bones with longer necks. This unintendedly supports the concept of avoiding boundary effects by designing long samples [10]. The greatest improvement in the value of the ratio, however, comes from the difference in the

ratio of the widths (β). In fact, as can be observed from Figure 20, ratios of almost one (0.95) can be achieved when the width of the dog bone is only a small fraction of the width of the shoulders ($\alpha = 0.125, 0.250$). Figure 21 further supports the use of these ratios, by showing the influence of the ratio of the widths (β) on the ratio between the target and boundary condition stresses. Dog bone samples with a ratio of widths equal to one-eight (1/8 or 0.125) give rise to an almost two-fold increase in the stress ratio, as compared to variants with a ratio of widths equal to one-fourth (1/4 or 0.250). From Figures 20-23, the optimum dog bone sample can be defined as a variant of $\alpha = 0.5$ & $\beta = 0.125$. The dog bone sample should give rise to the ratios $\frac{\sigma_t}{\sigma_{bc}} = 0.944$ & $\frac{\sigma_t}{\sigma_{bc}} = 4.6$. For a better understanding of these graphs, please refer to Figure 24.

Cruciform variants

The two principal components of the stress (σ_{xx}, σ_{yy}) were measured within four (4) ROIs, at three (3) simulation states (5, 15, and 25). For each component of the stress, three ratios were calculated. Given that understanding the effect of curvatures or arches, as means for reducing intensities, was an objective of studying cruciform variants, the ratios with respect to the intensity and maximum stress were measured. In this case, the region of the expected intensity shifted toward the point on the curvature closest to the original right corner (created at the intersection of the cruciform arms). As shown in Figures 25-30, the use of three-point arches was effective at increasing the value of the target to intensity ratio ($\frac{\sigma_t}{\sigma_{si}}$), regardless of the simulation state and/or time. As this ratio increased however, stress shifted towards the gripped boundary of the sample, producing an inversely proportional decrease in the ratio of the target to the boundary ($\frac{\sigma_t}{\sigma_{bc}}$). Although the

intersection between these two ratios (Figure 25-30) could be considered as an indicator for an optimum geometric variant, this criteria does not correlate with high target to maximum stress ratio. The latter criteria was found to be relatively independent to other ratios while dependent by the simulation time. At short simulation times, peak values of the ratios are achieved in variants defined by $0.5<R<0.75$. As the simulation continues, peaks are clearer in variants with $R=1.5$ (half the maximum possible radius). Although short simulation times are important, the behavior at tenths of second tends to be more homogeneous throughout the model as not much strain has been applied to the system. Therefore, it is safe to conclude that variants with $R=1.5$ are optimum. For a better understanding of these graphs, please refer to Figure 31.

Works Cited

[1] Y. C. Fung, Biomechanics, Mechanical Properties of Living Tissues, 2nd ed., New York, New York: Springer, 1993.

[2] Y. Lanir and Y. C. Fung, "Two-Dimensional Mechanical Properties of Rabbit Skin I: Experimental System," *Journal of Biomechanics,* vol. 7, pp. 29-34, 1974.

[3] Y. Lanir and Y. C. Fung, "Two-Dimensional Mechanical Properties of Rabbit Skin II: Experimental Results," *Journal of Biomechanics,* vol. 7, pp. 171-182, 1974.

[4] Y. Lanir, "Constitutive equations for fibrous connective tissues," *Journal of Biomechanics,* vol. 16, no. 1, pp. 1-12, 2 April 1982.

[5] J. D. Humphrey and F. C. P. Yin, "A new constitutive formulation for characterizing the machanical behavior of soft tissues," *Biophysical Journal,* vol. 52, pp. 563-570, October 1987.

[6] J. D. Humphrey and F. C. P. Yin, "On Constitutive Relations and Finite Deformations of Passive Cardiac Tissue: I. A Pseudostrain-Energy Function," *Journal of Biomechanical Engineering,* vol. 109, pp. 298-304, 1987.

[7] Y. Lanir, O. Lichtenstein and O. Imanuel, "Optimal Design of Biaxial Tests for Structural Material Characterization of Flat Tissues," *Journal of Biomechanical Engineering,* vol. 118, pp. 41-47, February 1996.

[8] M. S. Sacks and W. Sun, "Multiaxial Mechanical Behavior of Biological Materials," *Annual Reviews of Biomedical Engineering,* no. 5, pp. 251-284, 2003.

[9] ASTM Standard D412-06a, "Standard Test Methods for Vulcanized Rubber and Thermoplastic Elastomers - Tension," ASTM International, West Conshohocken, PA, 2013.

[10] W. Sun and M. M. Sacks, "Effects of Boundary Conditions on the Estimation of the Planar Biaxial Mechanical Properties of Soft Tissues," *Journal of Biomechanics,* vol. 127, no. 709, August 2005.

[11] S. A. Maas, B. J. Ellis, G. A. Ateshian and J. A. Weiss, "FEBio: Finite Elements for Biomechanics," *Journal of Biomechanical Engineering,* vol. 134, 22 January 2012.

[12] G. A. Hozapfel, T. C. Gasser and R. W. Ogden, "Hyperelastic modeling of arterial layers with distributed collagen fibre orientations," *Journal of The Royal Society Interface,* vol. 3, pp. 15-35, 28 September 2005.

[13] G. A. Ateshian, V. Rajan, N. O. Chahine, C. E. Canal and C. T. Hung, "Modeling the Matrix of Articular Cartilage Using a Continuous Fiber Angular Distribution Predicts Many Observed Phenomena," *ASME Journal of Biomechanical Engineering*, vol. 131, June 2009.

[14] Sandia National Laboratories, "Cubit 15.0 User Documentation," 2015.

[15] G. Ateshian, "Anisotropy of Fibrous Tissues in Relation to the Distribution of Tensed and Buckled Fibers," *Journal of Biomechanics*, vol. 129, pp. 240-249, April 2007.

[16] E. Gentleman, A. N. Lay, D. A. Dickerson, E. A. Nauman, G. A. Livesay and K. C. Dee, "Mechanical characterization of collagen fibers and scaffolds for tissue engineering," *Biomaterials*, no. 24, pp. 3805-3813, 24 March 2003.

[17] L. Bozec and M. Horton, "Topography and mechanical properties of single molecules of type I collagen using atomic force microscopy," *Biophysical Journal*, vol. 88, pp. 4223-4231, June 2005.

[18] E. B. Tadmor, R. E. Miller and R. S. Ellioot, Continuum Mechanics and Thermodynamics: From Fundamental Concepts to Governing Equations, Cambridge University Press., 2011.

[19] G. A. Holzapfel, Nonlinear Solid Mechanics: A Continuum Approach for Engineering, West Sussex: John Wiley and Sons Ltd., 2000.

[20] S. Maas, D. Rawlins, J. Weiss and G. Ateshian, "FEBio: Finite Elements for Biomechanics - Theory Manual," Salt Lake City, 2014.

[21] S. Maas, D. Rawlins, J. Weiss and G. Ateshian, "FEBio: Finite Elements for Biomechanics - Users Manual," Salt Lake City, 2014.

[22] Center for Research in Education and Simulation Technologies (CREST), "What is CREST?," [Online]. Available: http://www.crest.umn.edu/. [Accessed 5 April 2015].

[23] J. C. Simo and R. L. Taylor, "Quasi-incompressible finite elasticityin principal stretches: Continuum basis and numerical algorithms," *Computer Methods in Applied Mechanics and Engineering*, no. 85, pp. 273-310, 1991.

Appendices

Appendix A – Relevant and Supplemental Figures

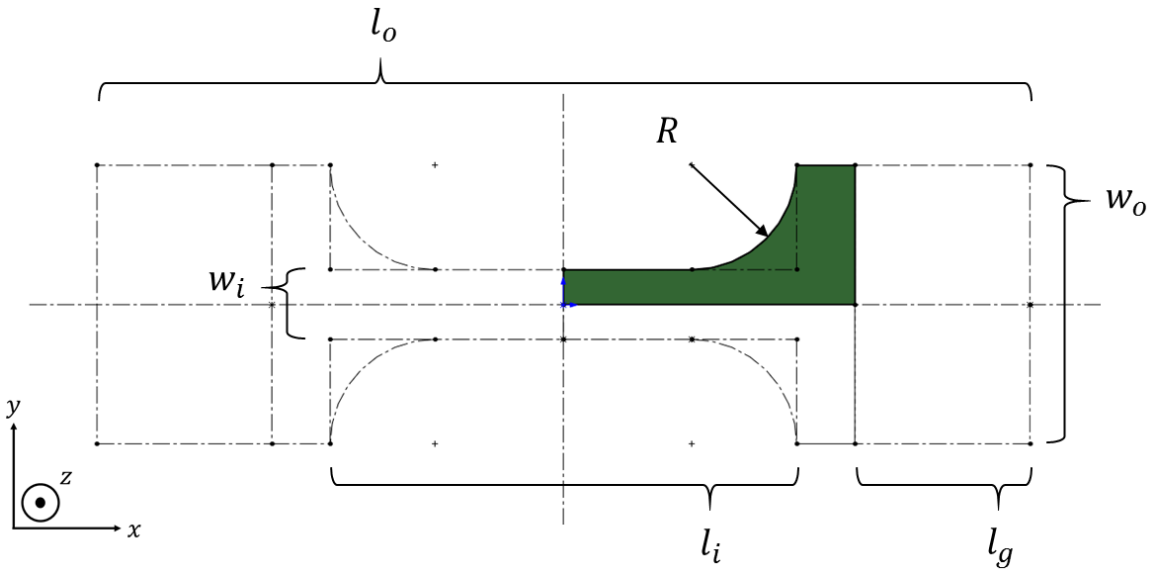

Figure 1: The dog bone or dumbbell specimen. The dog bone or dumbbell is drawn from a rectangle of length l_o and width w_o. An inner rectangle, of length l_i and width w_i, outlines the neck region of the dog bone or dumbbell. The sharp corners are then smoothed using curves of radius R. The remaining dimension l_g, describes the length of the area used for sample gripping.

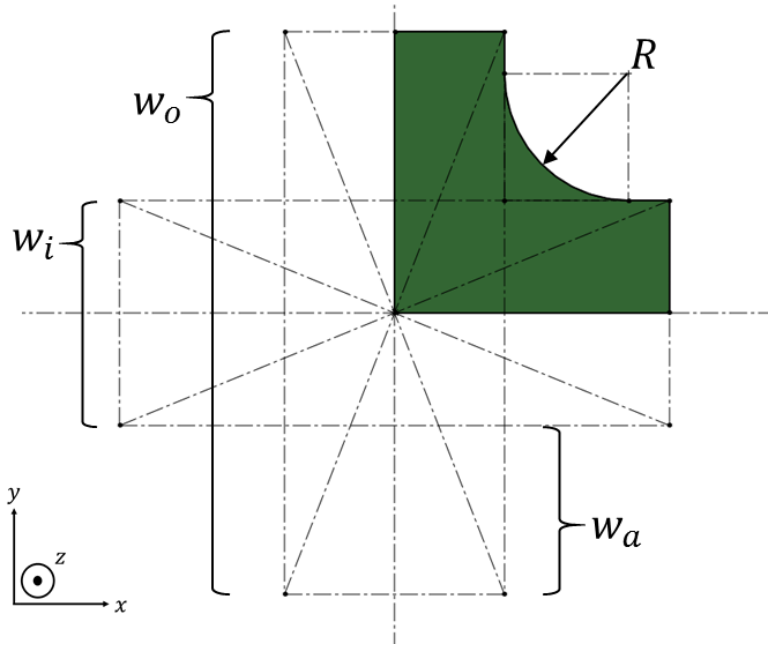

Figure 2: The cruciform specimen. The cruciform was drawn from a square of width w_o. The arms of the cruciform extend from an inner square of width w_i, for a length of w_a. The sharp corners are then smoothed using curves of radius R.

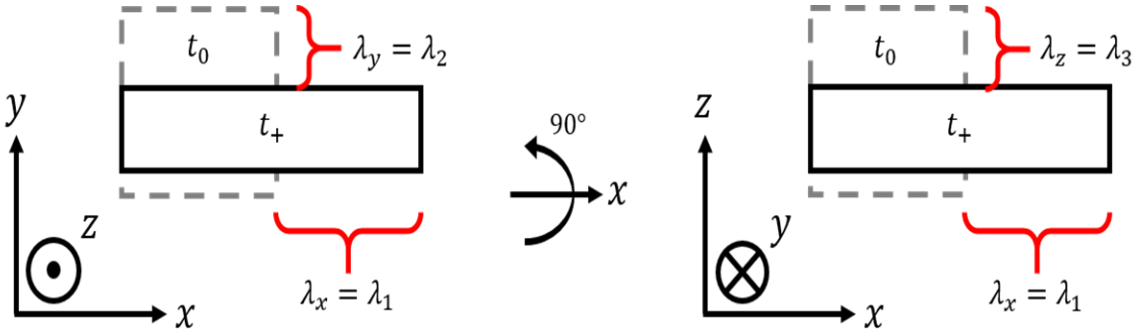

Figure 3: Graphic representation of an isotropic material undergoing uniaxial, tensile deformation. The undeformed (t_0) and the deformed (t_+) configuration of the material are shown in both coordinate perspectives. The graphics on the left show the $X-Y$ $(1-2)$ plane, whereas the graphics on the right show the $X-Z$ $(1-3)$ plane of the deformation. Logically, a 90° rotation about the X (1) axis is needed to move between perspectives. In both perspectives, the stretch ratios for the corresponding plane are shown. While the material undergoes an extension in X (1), equivalent contractions (or shortening) occur in Y, Z $(2,\ 3)$, so that $\lambda_y = \lambda_z$ $(\lambda_2 = \lambda_3)$.

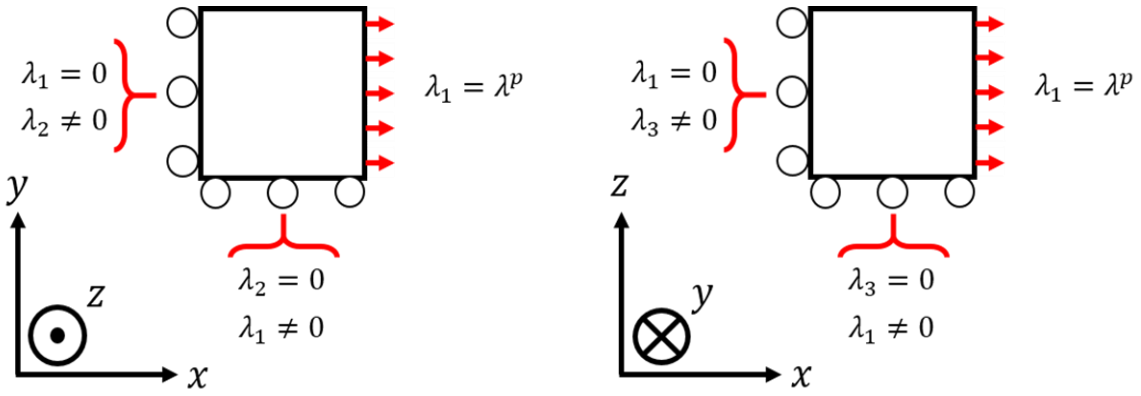

Figure 4: Graphic representation of the boundary conditions needed, within the FEA code, to simulate an ideal uniaxial deformation. As in previous pictures, two perspectives are shown to encompass the entirety of the three-dimensional space. In each case (left or right) rollers allow for sliding of the surface along coplanar or parallel directions, while constraining movement along the surface normal. Note that the stretch ratios (λ_i) are used to represent the stretch at the boundaries.

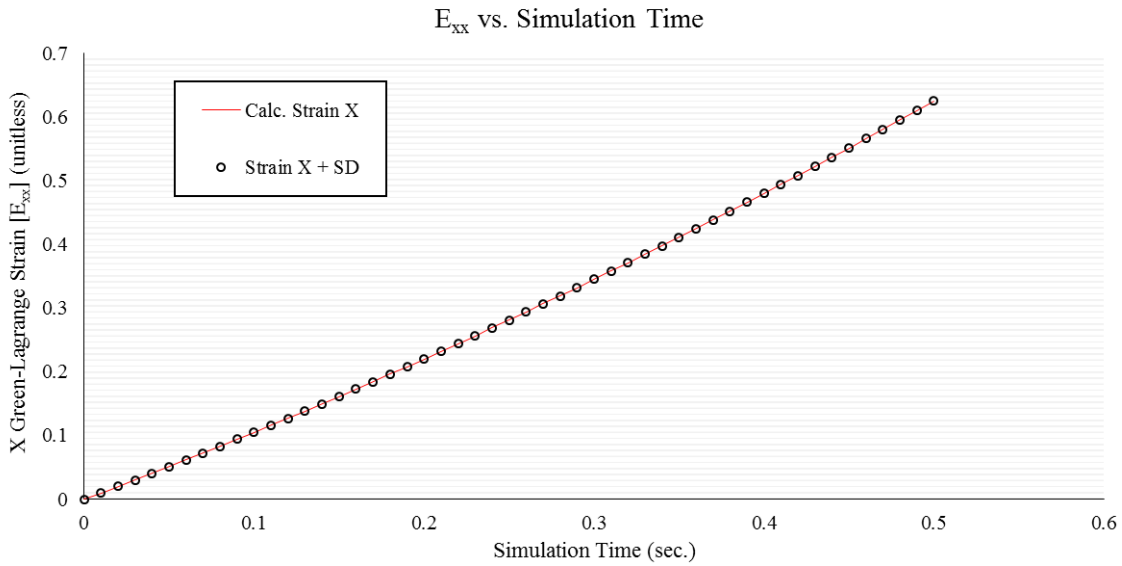

Figure 5: Comparison between calculated and simulated Green-Lagrange strain in the direction of pull X(1)(E_{xx}). Simulated results consisted of the average strain among all the elements of the mesh (N=1000). The standard deviation was plotted as the error for each measurement.

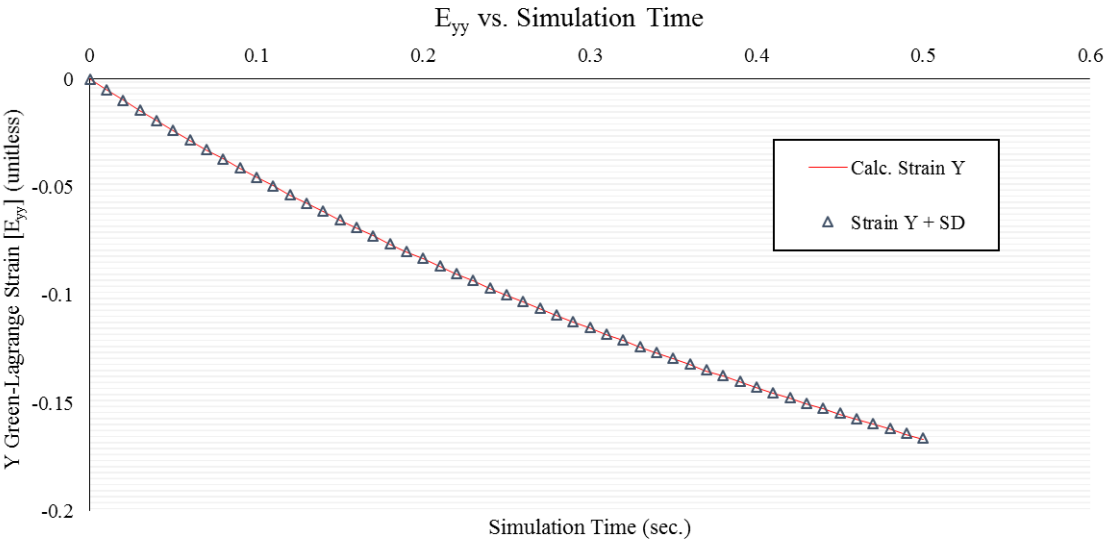

Figure 6: Comparison between calculated and simulated Green-Lagrange strain in Y (2) (E_{yy}). Simulated results consisted of the average strain among all the elements of the mesh (N=1000). The standard deviation was plotted as the error for each measurement.

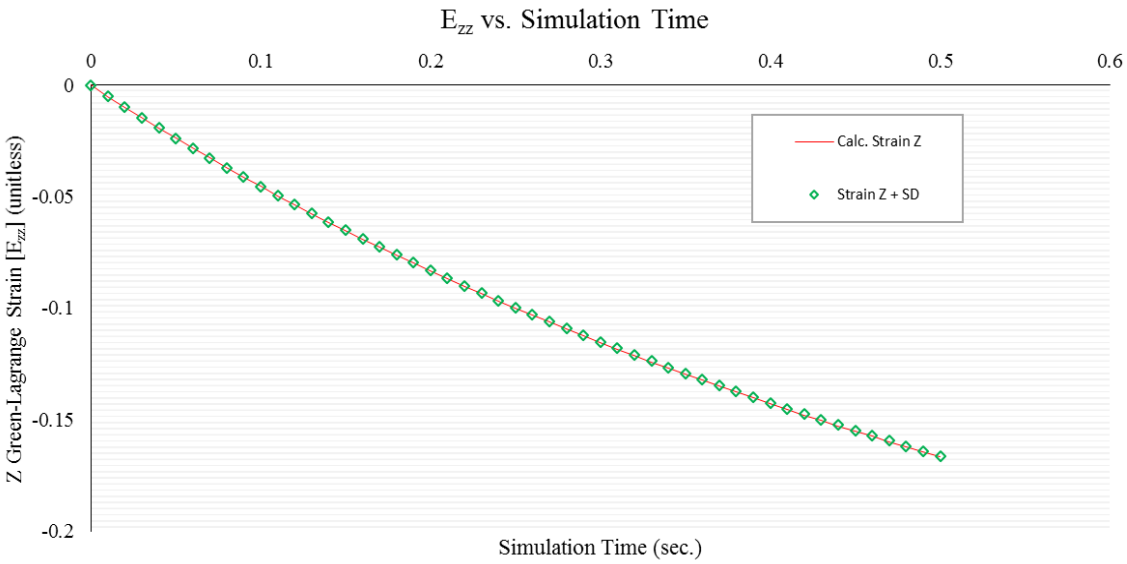

Figure 7: Comparison between calculated and simulated Green-Lagrange strain in Z (3) (E_{zz}). Simulated results consisted of the average strain among all the elements of the mesh (N=1000). The standard deviation was plotted as the error for each measurement.

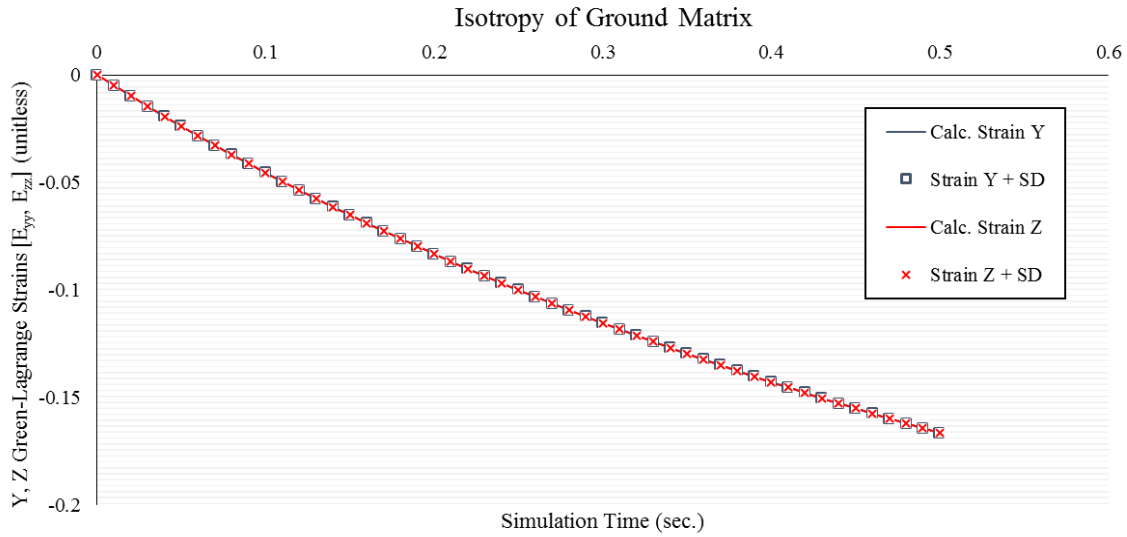

Figure 8: Comparison between calculated and simulated Green-Lagrangian strains in $Y(2)(E_{yy})$ and $Z(3)(E_{zz})$. The equivalence between the two orientations corroborated the hypothesized isotropic behavior of the material. Simulated results consisted of the average strain among all the elements of the mesh (N=1000). The standard deviation was plotted as the error for each measurement.

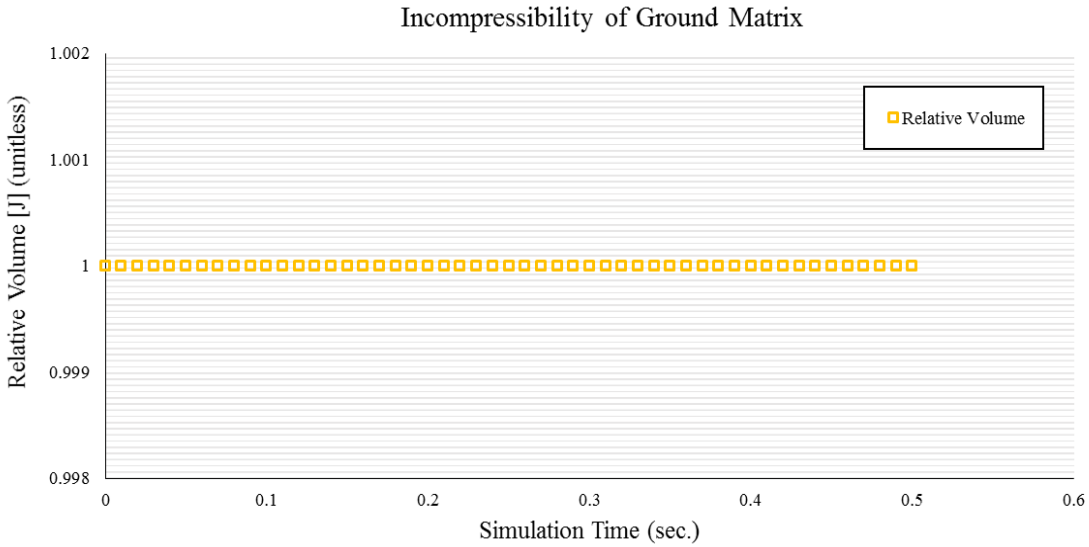

Figure 9: Incompressibility of Ground Matrix. The relative volume (volume change) of the ground matrix material was tracked while undergoing uniaxial, tensile deformation. Throughout the experiment, the volume of the material was conserved (J=1).

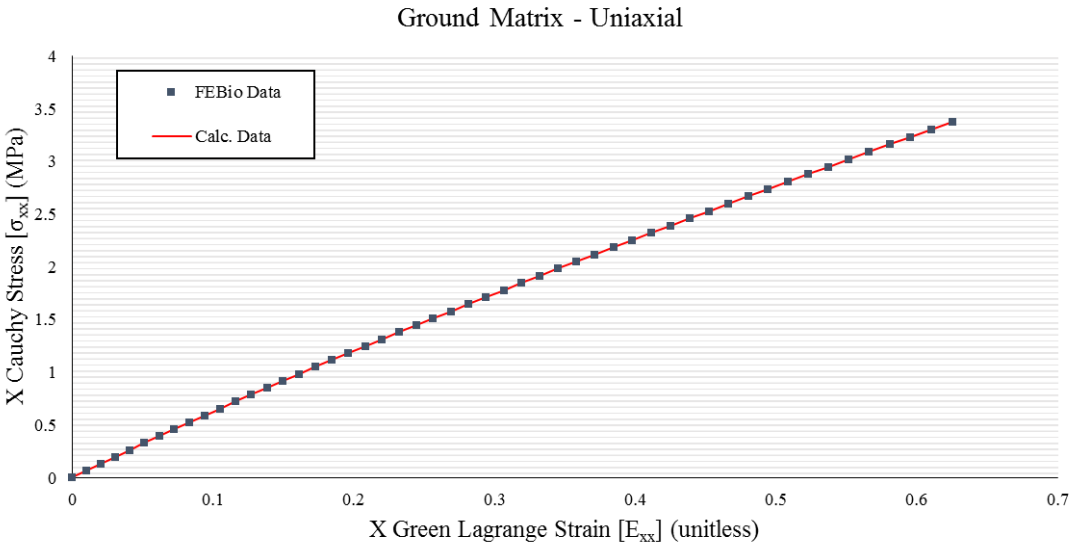

Figure 10: Stress-strain comparison between the FEA and the calculated data, under uniaxial deformation kinematics. The FEBio results were further compared with the idea Mooney-Rivlin material undergoing uniaxial deformation.

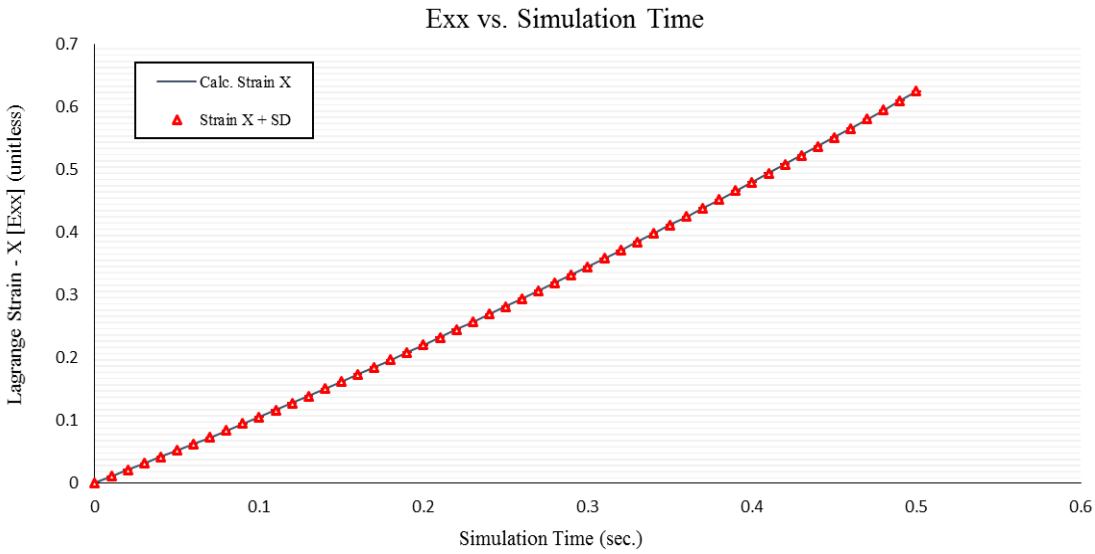

Figure 11: Comparison between calculated and simulated Green-Lagrange strain in the direction of pull $X(1)(E_{xx})$. Simulated results consisted of the average strain among all the elements of the mesh (N=1000). The standard deviation was plotted as the error for each measurement.

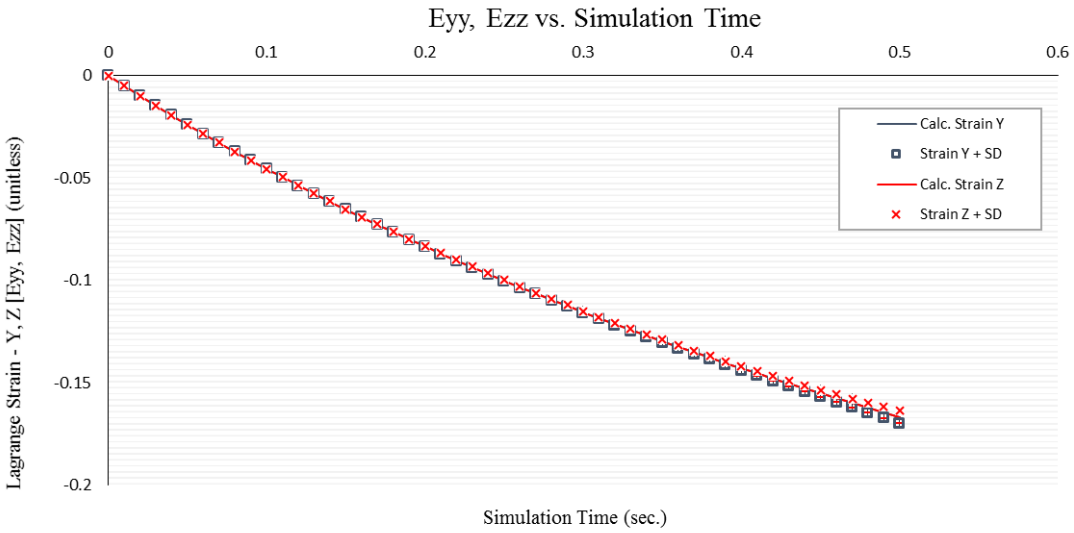

Figure 12: Comparison between calculated and simulated Green-Lagrangian strains in $Y(2)(E_{yy})$ and $Z(3)(E_{zz})$. The equivalence between the two orientations corroborated the hypothesized isotropic behavior of the material. Even in the presence of fibers, isotropy holds along the perpendicular plane. In this situation, the material can be better described as transversely isotropic. Simulated results consisted of the average strain among all the elements of the mesh (N=1000). The standard deviation was plotted as the error for each measurement.

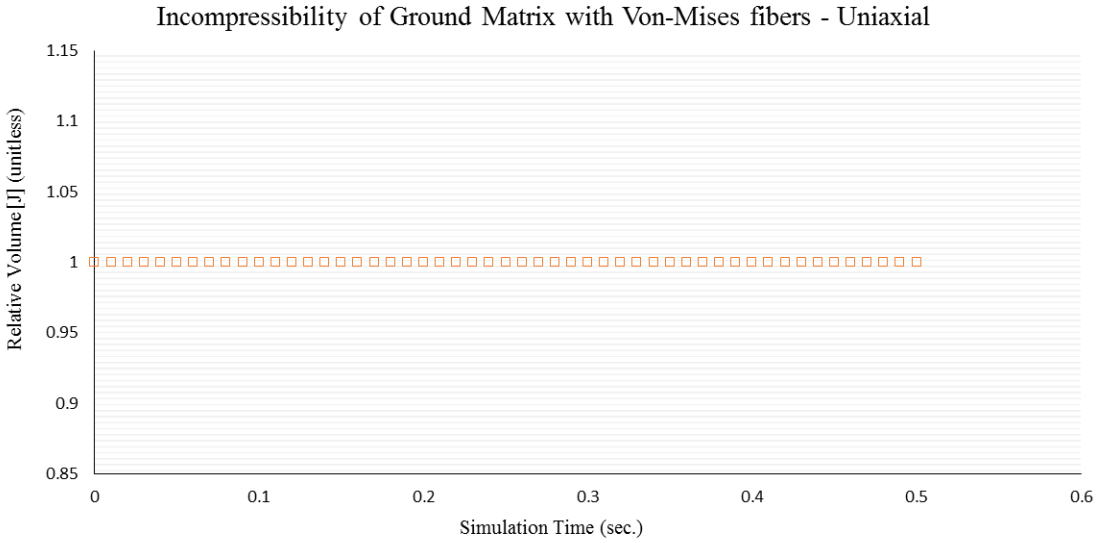

Figure 13: Incompressibility of Ground Matrix with Von-Mises fiber distribution. The relative volume (volume change) of the ground matrix material was tracked while undergoing uniaxial, tensile deformation. Throughout the experiment, the volume of the material was conserved (J=1).

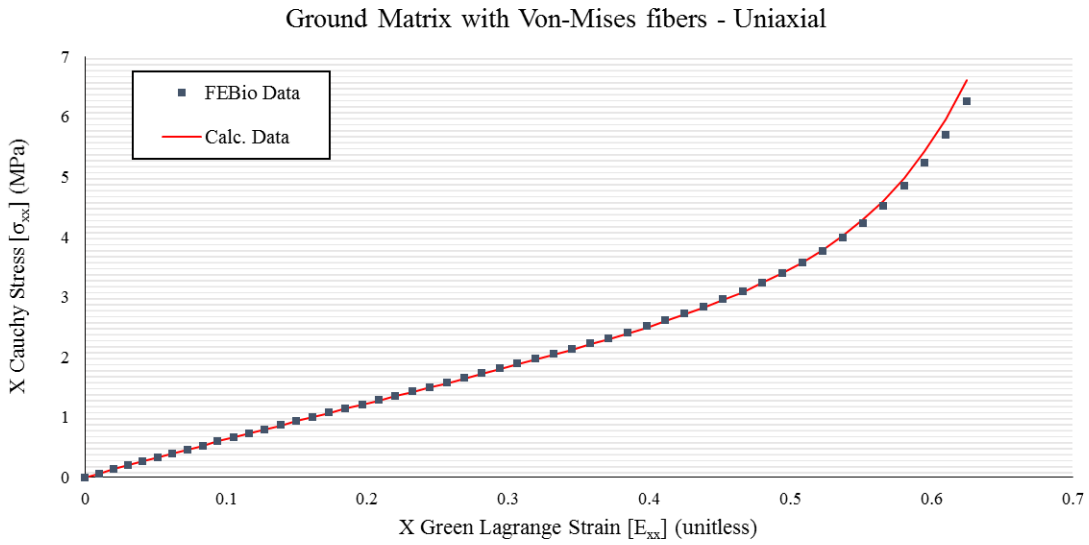

Figure 14: Stress-strain comparison between the FEA and the calculated data, under uniaxial deformation kinematics. The FEBio results were compared to the structural model composed of a Mooney-Rivlin ground matrix and a single Von-Mises fiber distribution. The material was mechanically stimulated along the direction of highest fiber concentration.

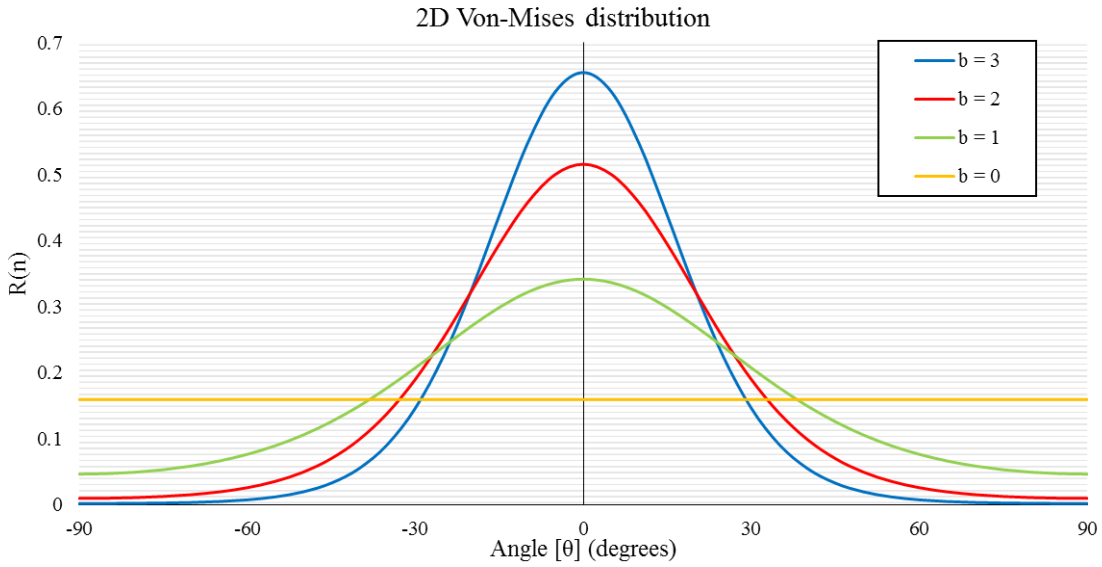

Figure 15: Two-dimensional (2D) Von-Mises distribution for fibers. The concentration factor b dictates the form of the distribution, including the maximum value of $R(n)$. When $b = 0$, an isotropic distribution of fibers exists within the material.

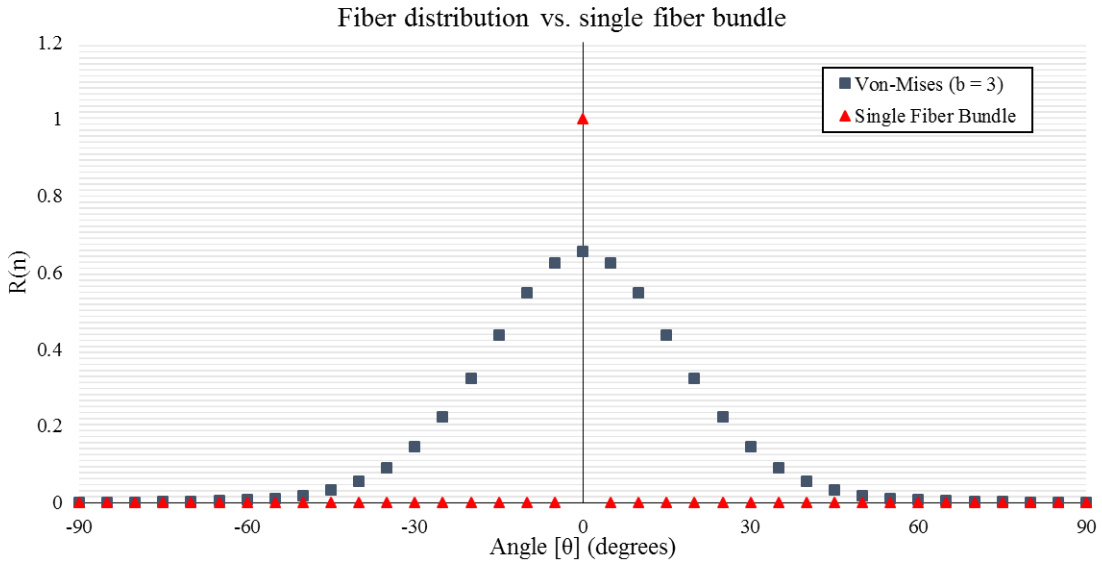

Figure 16: Comparison between a two-dimensional (2D) Von-Mises distribution ($b = 3$) and a single fiber bundle. Single fibers have the same effect as discontinuities within the material's continuum. These abrupt changes challenge the convergence of the FEA.

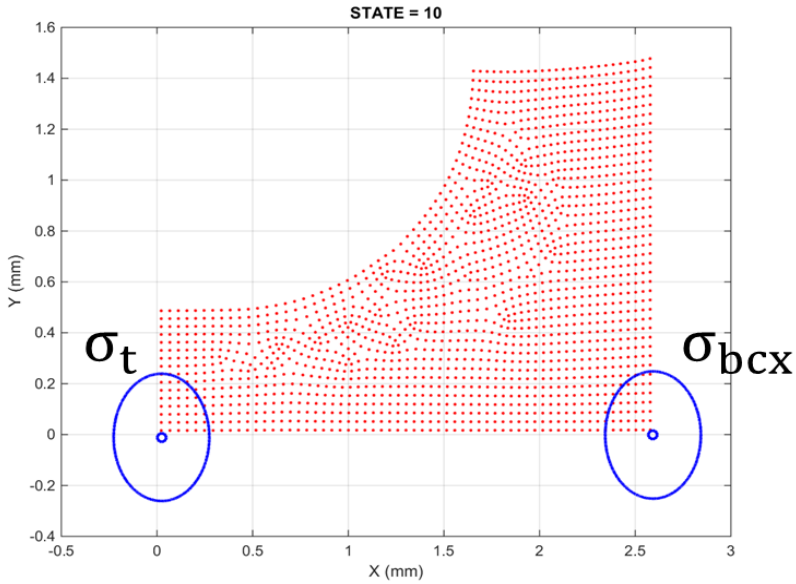

Figure 17: Regions of interest (ROIs) specific to dog bone variants. The figure was obtained from the Objective Partitioning algorithm as means of visually validating the correct dimensions and locations of the ROIs. Distortions are due to the scaling of the graph. In the case of the dog bone sample, only two ROIs are needed for analysis.

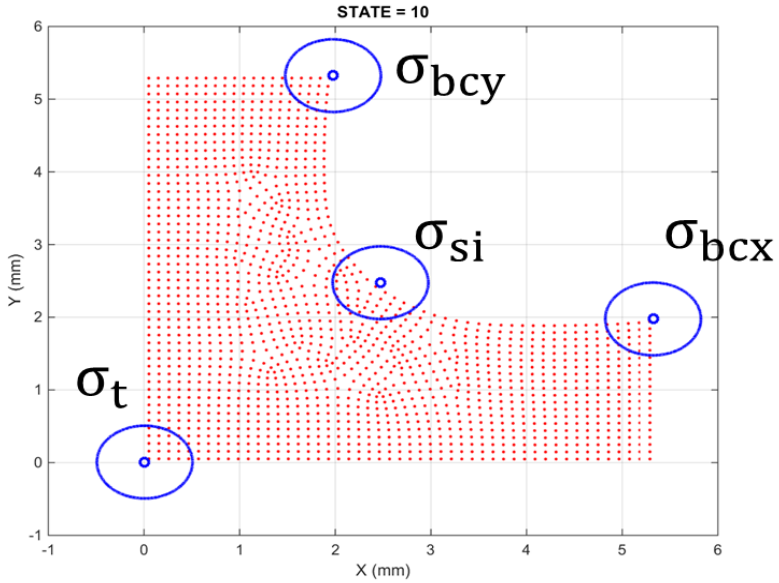

Figure 18: Regions of interest (ROIs) specific to cruciform variants. The figure was obtained from the Objective Partitioning algorithm as means of visually validating the correct dimensions and locations of the ROIs. Distortions are due to the scaling of the graph. Four (4) ROIs are needed for the proper analysis of cruciform variants.

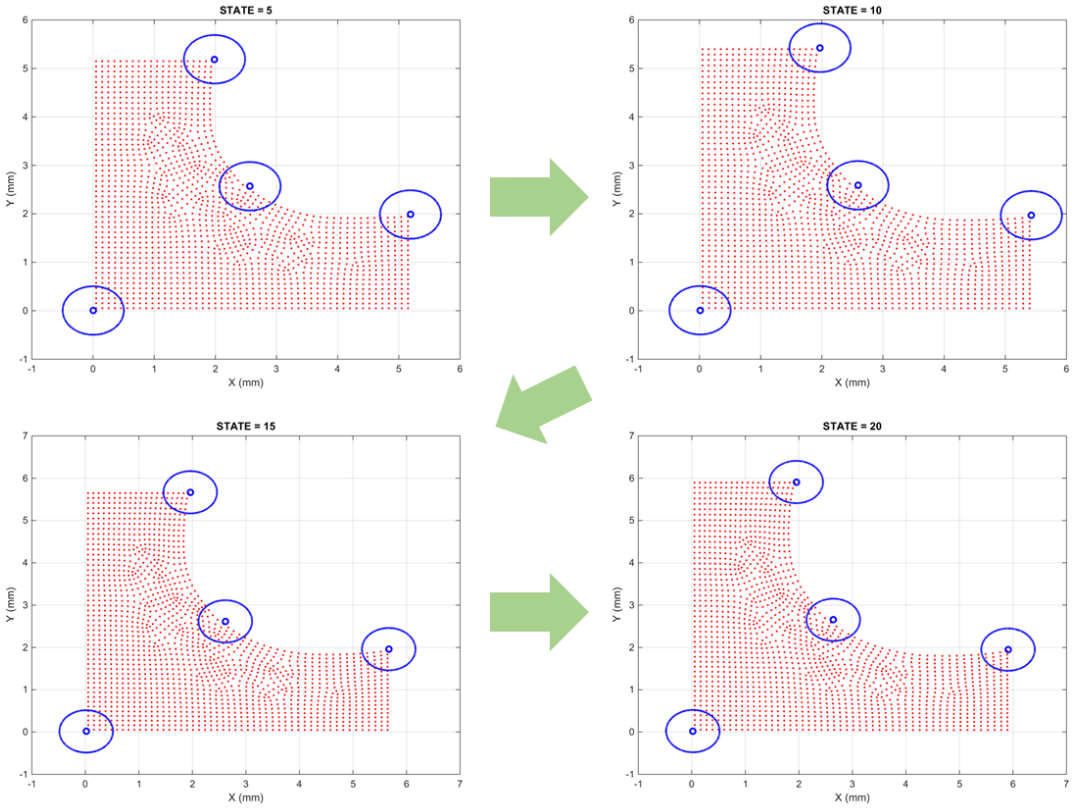

Figure 19: Objective Partitioning visual output. Visualization routines were designed to ensure that ROIs tracked or followed the deformation of the volume, according to the deformation mapping.

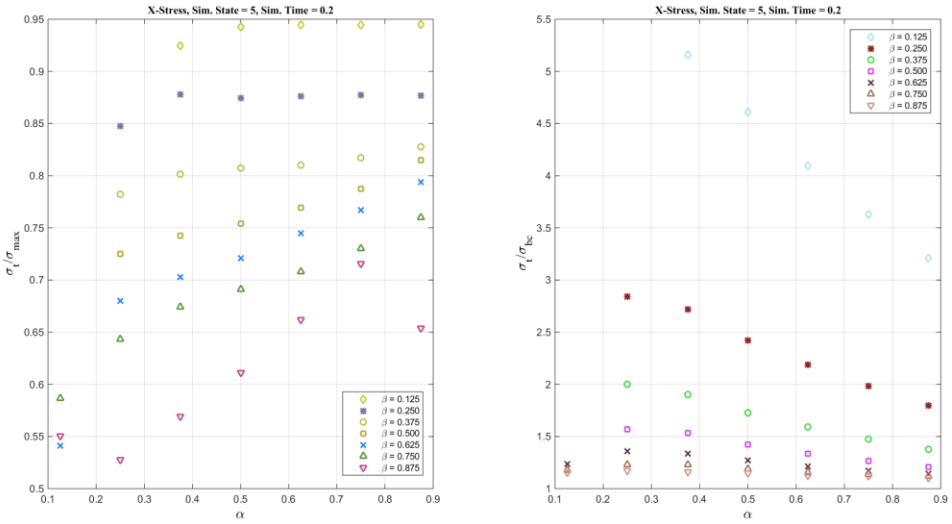

Figure 20: Dog bone variant analysis results (Simulation State 5, Time = 0.2 sec.). The ratio of X-stress between the target region and the maximum is shown on the left. The ratio of X-stress between the target region and the boundary condition is shown on the right. The ratios are plotted against α, the ratio of the lengths, while each data series represents a different value of β, the ratio of the widths.

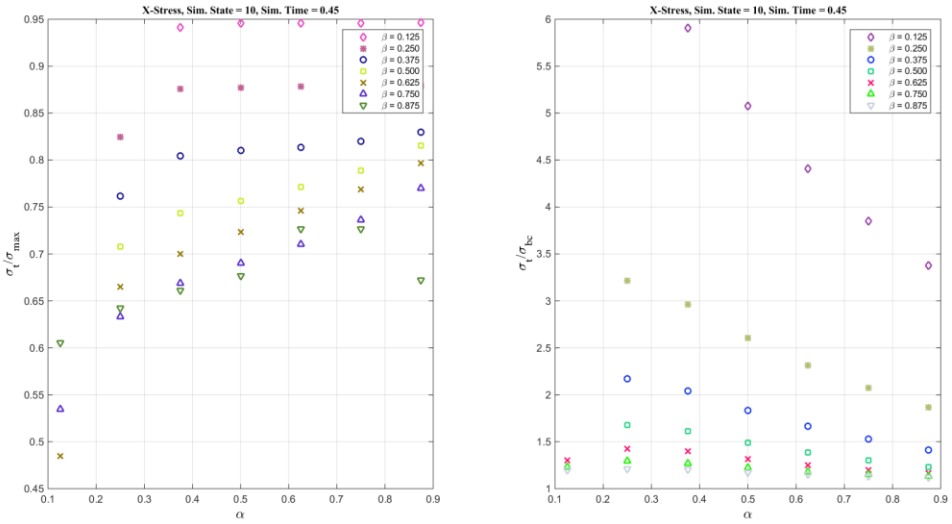

Figure 21: Dog bone variant analysis results (Simulation State 10, Time = 0.45 sec.). The ratio of X-stress between the target region and the maximum is shown on the left. The ratio of X-stress between the target region and the boundary condition is shown on the right. The ratios are plotted against α, the ratio of the lengths, while each data series represents a different value of β, the ratio of the widths.

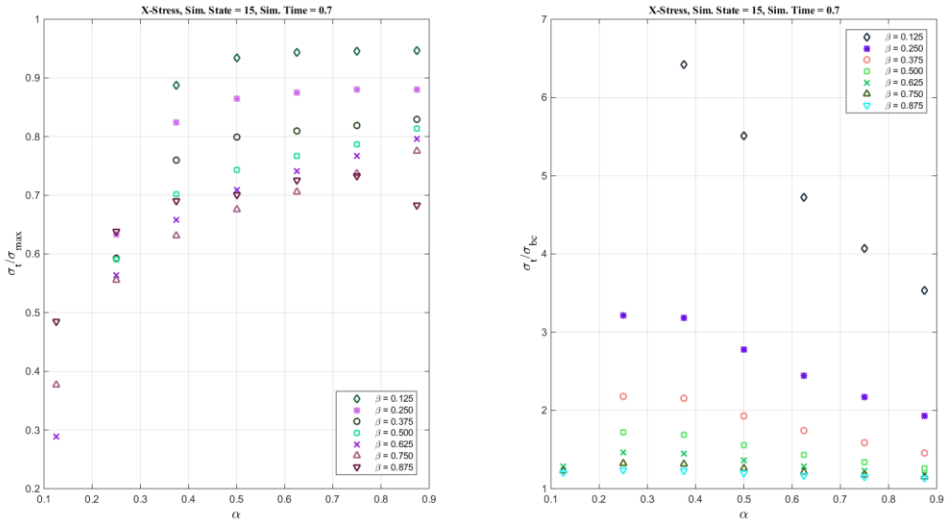

Figure 22: Dog bone variant analysis results (Simulation State 15, Time = 0.7 sec.). The ratio of X-stress between the target region and the maximum is shown on the left. The ratio of X-stress between the target region and the boundary condition is shown on the right. The ratios are plotted against α, the ratio of the lengths, while each data series represents a different value of β, the ratio of the widths.

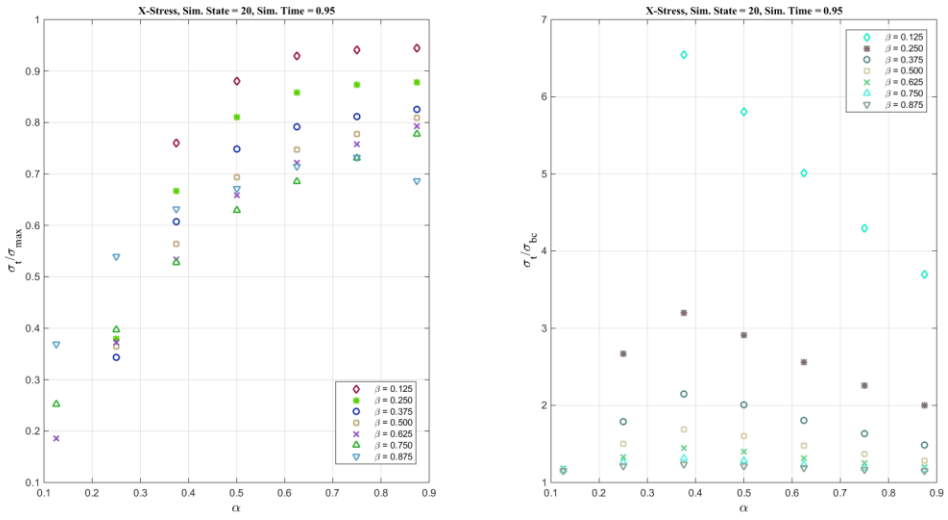

Figure 23: Dog bone variant analysis results (Simulation State 20, Time = 0.95 sec.). The ratio of X-stress between the target region and the maximum is shown on the left. The ratio of X-stress between the target region and the boundary condition is shown on the right. The ratios are plotted against α, the ratio of the lengths, while each data series represents a different value of β, the ratio of the widths.

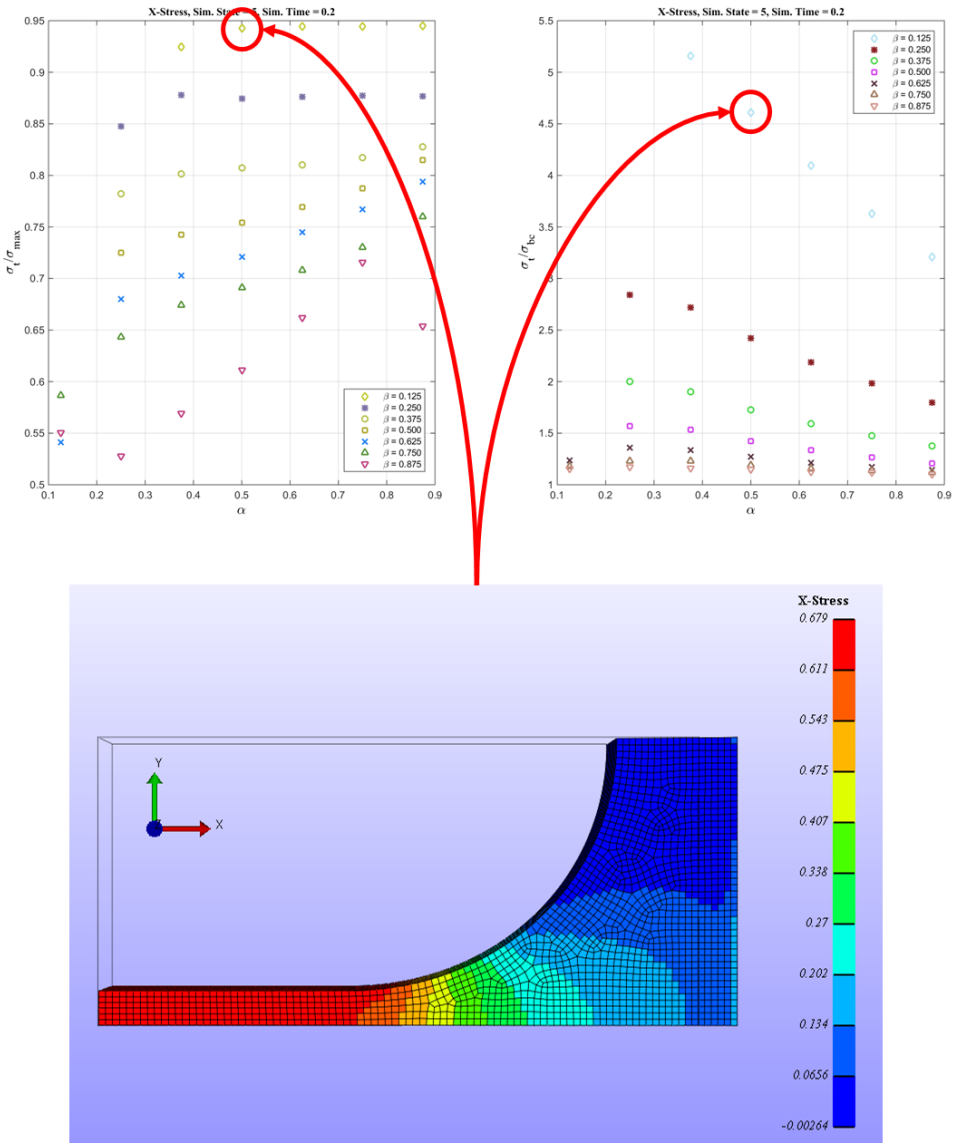

Figure 24: Dog bone effective variant. Using Figures 20-23, the most effective geometric variant of the dog bone or dumbbell sample can be identified. Note that, currently, the selection is made and validated by inspection of the graphs and FEA visualization.

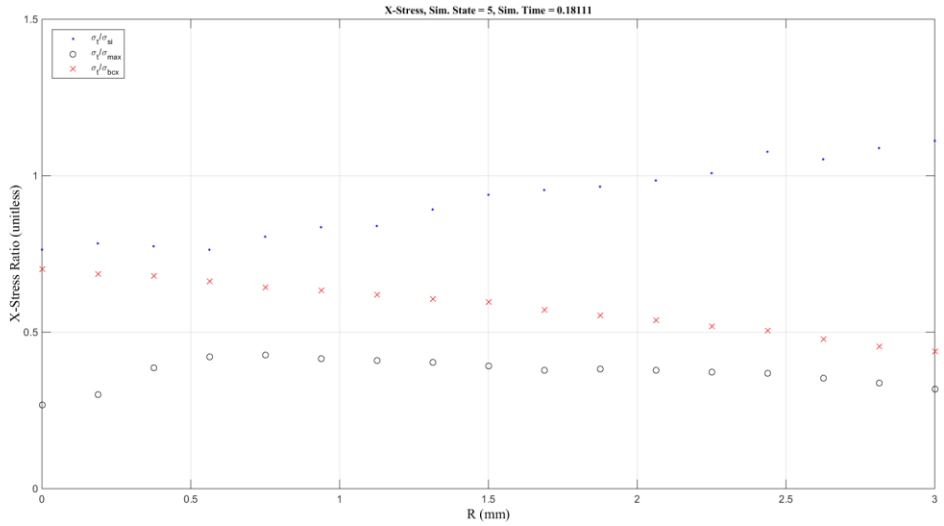

Figure 25: Cruciform variant analysis results (X-Stress, Simulation State 5, Time = 0.1811 sec.). The ratio of X-stress between the target region and the intensity, between the target region and the maximum stress, and between the target region and the boundary are plotted together. The ratios are plotted against the only varying dimension across the models, the radius of curvature (R) defining the three-point arch.

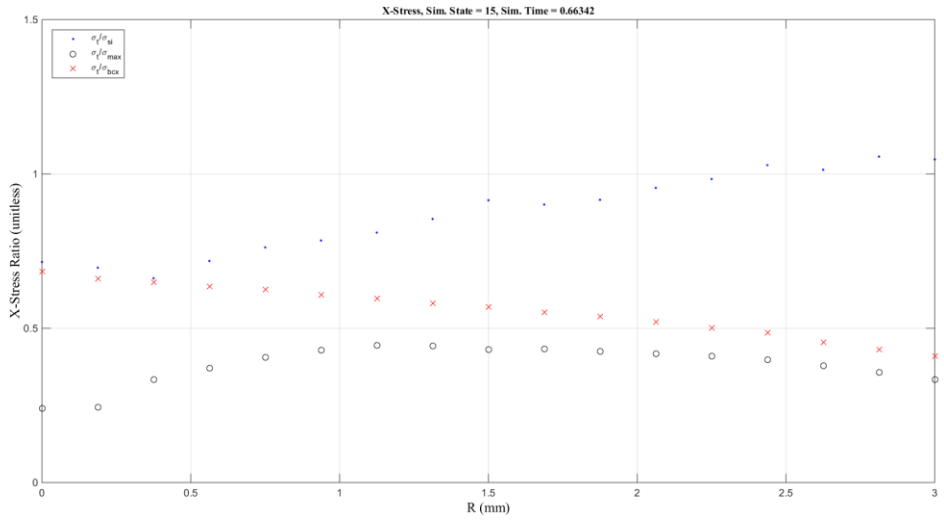

Figure 26: Cruciform variant analysis results (X-Stress, Simulation State 15, Time = 0.66342 sec.). The ratio of X-stress between the target region and the intensity, between the target region and the maximum stress, and between the target region and the boundary are plotted together. The ratios are plotted against the only varying dimension across the models, the radius of curvature (R) defining the three-point arch.

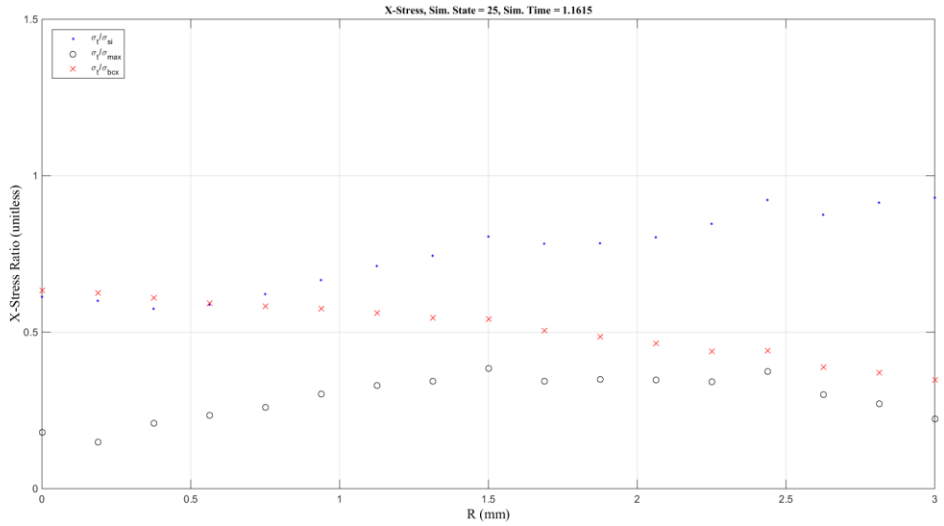

Figure 27: Cruciform variant analysis results (X-Stress, Simulation State 25, Time = 1.1615 sec.). The ratio of X-stress between the target region and the intensity, between the target region and the maximum stress, and between the target region and the boundary are plotted together. The ratios are plotted against the only varying dimension across the models, the radius of curvature (R) defining the three-point arch.

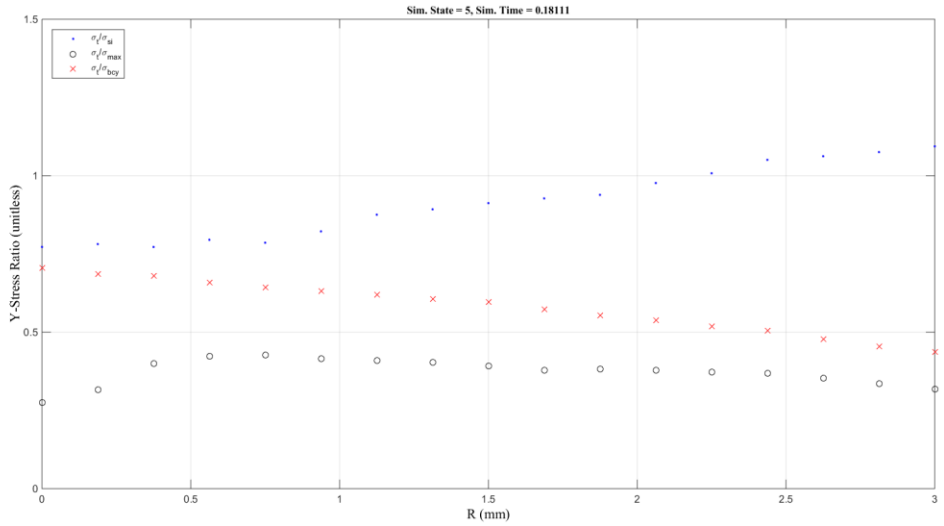

Figure 28: Cruciform variant analysis results (Y-Stress, Simulation State 5, Time = 0.1811 sec.). The ratio of Y-stress between the target region and the intensity, between the target region and the maximum stress, and between the target region and the boundary are plotted together. The ratios are plotted against the only varying dimension across the models, the radius of curvature (R) defining the three-point arch.

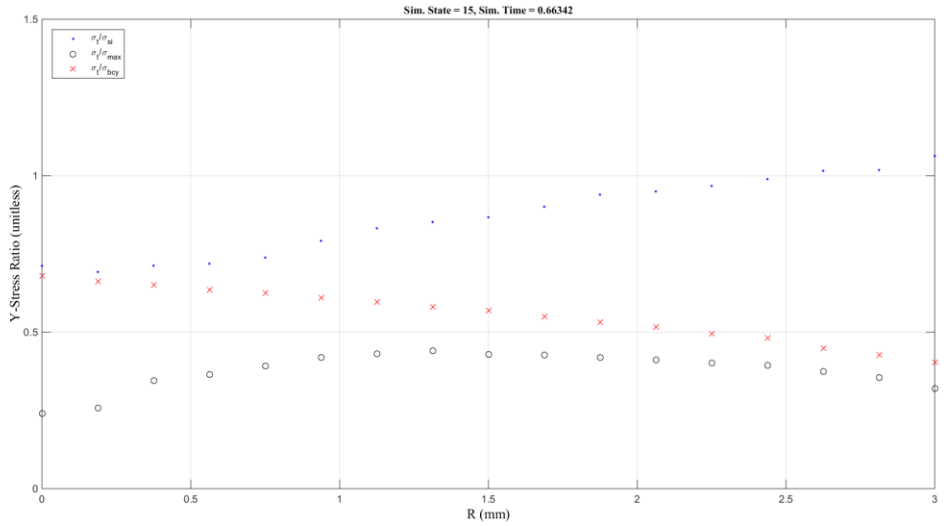

Figure 29: Cruciform variant analysis results (Y-Stress, Simulation State 15, Time = 0.66342 sec.). The ratio of Y-stress between the target region and the intensity, between the target region and the maximum stress, and between the target region and the boundary are plotted together. The ratios are plotted against the only varying dimension across the models, the radius of curvature (R) defining the three-point arch.

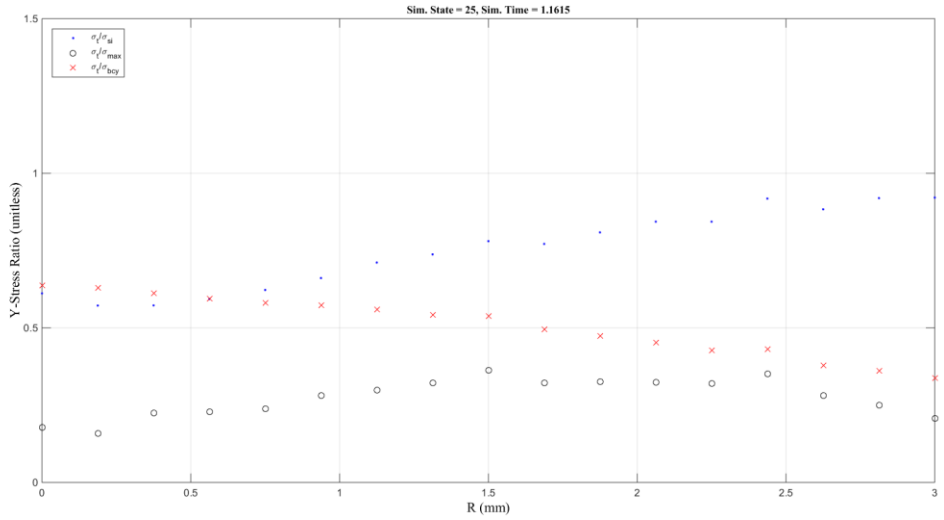

Figure 30: Cruciform variant analysis results (Y-Stress, Simulation State 5, Time = 0.1811 sec.). The ratio of Y-stress between the target region and the intensity, between the target region and the maximum stress, and between the target region and the boundary are plotted together. The ratios are plotted against the only varying dimension across the models, the radius of curvature (R) defining the three-point arch.

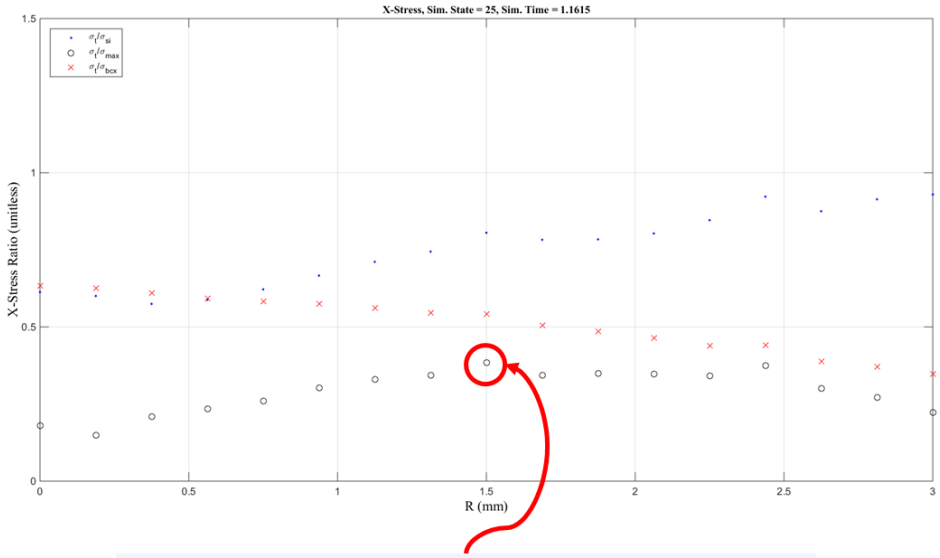

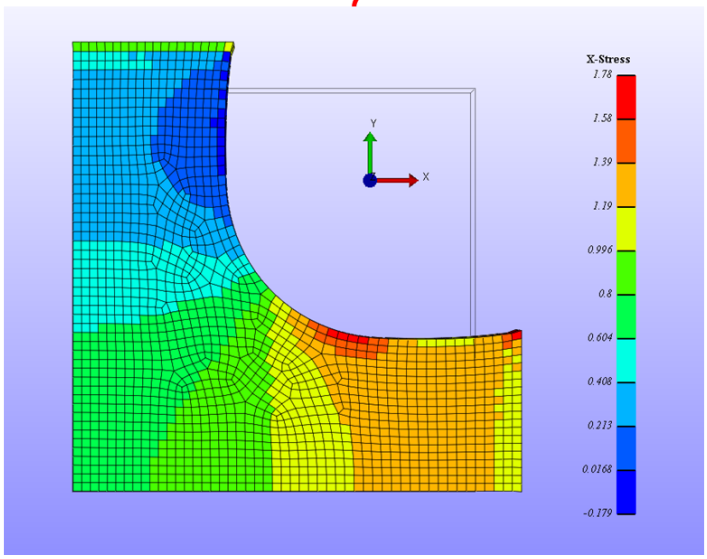

Figure 31: Cruciform effective variant. Using Figures 25-30, the most effective geometric variant of the cruciform sample can be identified. Note that, currently, the selection is made and validated by inspection of the graphs and FEA visualization.

Appendix B – Equations and derivations

∇ Instead of presenting a comprehensive summary of all kinematic definitions and formulations, this section focuses on supporting the mathematical derivation of the structural model used in this study. The reader is encouraged to explore the foundations of these derivations from the references section [1, 18, 19].

∇ Additional definitions, specific to equations used within FEBio and implemented throughout the study, can be consulted within both “Theory” and “Users” manuals [11, 20, 21].

Mooney-Rivlin isotropic, incompressible material model for the Ground Matrix

The strain energy function of an incompressible, Mooney-Rivlin material is given by;

$$W_{MR}(I_1, I_2) = c_1(I_1 - 3) + c_2(I_2 - 3);$$

Equation 1

Substituting for the material invariants I_1 and I_2, the same function can be presented in terms of the principal stretch ratios:

$$W_{MR}(\lambda_1, \lambda_2, \lambda_3) = c_1(\lambda_1^2 + \lambda_2^2 + \lambda_3^2 - 3) + c_2(\lambda_1^2\lambda_2^2 + \lambda_2^2\lambda_3^2 + \lambda_1^2\lambda_3^2 - 3);$$

Equation 2

From this form, the principal components of the 1st Piola Kirchhoff stress tensor (t) are derived.

$$t = \begin{bmatrix} 2c_1\lambda_1 + 2c_2\lambda_1(\lambda_2^2 + \lambda_3^2) & 0 & 0 \\ 0 & 2c_1\lambda_2 + 2c_2\lambda_2(\lambda_1^2 + \lambda_3^2) & 0 \\ 0 & 0 & 2c_1\lambda_3 + 2c_2\lambda_3(\lambda_1^2 + \lambda_2^2) \end{bmatrix};$$

Equation 3

This stress tensor can then be used to calculate the components of the Cauchy stress tensor (σ) [18, 1]. Where p represents the hydrostatic pressure within the material.

$$\sigma = \begin{bmatrix} 2c_1\lambda_1^2 + 2c_2\lambda_1^2(\lambda_2^2 + \lambda_3^2) & 0 & 0 \\ 0 & 2c_1\lambda_2^2 + 2c_2\lambda_2^2(\lambda_1^2 + \lambda_3^2) & 0 \\ 0 & 0 & 2c_1\lambda_3^2 + 2c_2\lambda_3^2(\lambda_1^2 + \lambda_2^2) \end{bmatrix} + pI;$$

Equation 4

Mooney-Rivlin model with uniaxial kinematics

Uniaxial kinematics were used for the validation of simulate uniaxial tensile experiments. First, the principal direction was equated to the direction of pull.

$$\lambda_1 = \lambda^*;$$

Equation 5

Material isotropy was established by equating the remaining directions in the plane perpendicular to the deformation.

$$\lambda_2 = \lambda_3;$$

Equation 6

Incompressibility, derived from the Deformation Gradient Tensor (F), was then used to define the λ_2, λ_3 in terms of λ_1.

$$\det \mathrm{F} = \mathrm{J} = \lambda_1\lambda_2\lambda_3 \equiv \lambda^*\lambda_2^2 = 1;$$

Equation 7

$$\lambda_2 = \lambda_3 = \frac{1}{\sqrt{\lambda^*}};$$

Equation 8

This definition was used to further simplify the components of the Cauchy Stress tensor (σ).

$$\sigma_{\mathrm{MR}} = \begin{bmatrix} 2c_1\lambda^{*2} + 2c_2\lambda^{*2}\left(\frac{1}{\lambda^*} + \frac{1}{\lambda^*}\right) & 0 & 0 \\ 0 & 2c_1\frac{1}{\lambda^*} + 2c_2\frac{1}{\lambda^*}\left(\lambda^{*2} + \frac{1}{\lambda^*}\right) & 0 \\ 0 & 0 & 2c_1\frac{1}{\lambda^*} + 2c_2\frac{1}{\lambda^*}\left(\lambda^{*2} + \frac{1}{\lambda^*}\right) \end{bmatrix} + \mathrm{pI};$$

Equation 9

In unconstrained uniaxial tests, where the plane perpendicular to the direction of pull deforms freely, stresses are zero on the unconstrained faces of the material.

$$\sigma_{22} = \sigma_{33} = 0;$$

Equation 10

This relation was used to derive the value of the hydrostatic pressure (p) within the material.

$$p = -2c_1\frac{1}{\lambda^*} - 2c_2\frac{1}{\lambda^*}\left(\lambda^{*^2} + \frac{1}{\lambda^*}\right);$$

Equation 11

Finally, the equation for the hydrostatic pressure (p) was substituted into the stress components corresponding to the direction of pull. Therefore, the correct form of the Cauchy Stress tensor (σ) was written as.

$$\sigma^*_{MR} = \begin{bmatrix} 2c_1\lambda^{*^2} + 2c_2\lambda^{*^2}\left(\frac{1}{\lambda^*} + \frac{1}{\lambda^*}\right) - 2c_1\left(\frac{1}{\lambda^*}\right) - 2c_2\left(\frac{1}{\lambda^*}\right)\left(\lambda^{*^2} + \frac{1}{\lambda^*}\right) & 0 & 0 \\ 0 & 0 & 0 \\ 0 & 0 & 0 \end{bmatrix};$$

Equation 12

Further simplification of the Cauchy Stress tensor (σ) leads to two (2) commonly used forms of the Mooney-Rivlin material model.

$$\sigma^*_{MR} = \begin{bmatrix} 2c_1\lambda^{*^2} + 2c_1\left(\lambda^{*^2} - \frac{1}{\lambda^*}\right) + 2c_2\left(\lambda^* - \frac{1}{\lambda^{*^2}}\right) & 0 & 0 \\ 0 & 0 & 0 \\ 0 & 0 & 0 \end{bmatrix};$$

Equation 13

Also presented as.

$$\sigma^*_{MR} = \begin{bmatrix} \left(2c_1 + \frac{2c_2}{\lambda^*}\right)\left(\lambda^{*^2} - \frac{1}{\lambda^*}\right) & 0 & 0 \\ 0 & 0 & 0 \\ 0 & 0 & 0 \end{bmatrix};$$

Equation 14

Mooney-Rivlin model with biaxial kinematics

Biaxial kinematics were used for the validation of simulate biaxial tensile experiments. First, the two principal orientations of pull were equated.

$$\lambda_1 = \lambda_2 = \lambda^*;$$

Equation 15

In the biaxial case, given that the deformation is controlled in two of the three planes, isotropy does not play an important role in the derivation process yet. On the other hand, incompressibility (Equation 7) is still used to calculate the deformation in the remaining orientation.

$$\lambda_3 = \frac{1}{\lambda^{*2}};$$

Equation 16

Similarly to the uniaxial case, this relation can then be used to simplify the Cauchy stress tensor (σ).

$$\sigma^*_{MR} = \begin{bmatrix} 2c_1\lambda^{*2} + 2c_2\lambda^{*2}\left(\lambda^{*2} + \frac{1}{\lambda^{*4}}\right) & 0 & 0 \\ 0 & 2c_1\lambda^{*2} + 2c_2\lambda^{*2}\left(\lambda^{*2} + \frac{1}{\lambda^{*4}}\right) & 0 \\ 0 & 0 & 2c_1\left(\frac{1}{\lambda^{*4}}\right) + 2c_2\left(\frac{1}{\lambda^{*4}}\right)\left(\lambda^{*2} + \lambda^{*2}\right) \end{bmatrix} + pI;$$

Equation 17

Given the kinematics of the experiment, three claims can be made about the equations above. First, given an isotropic model, the stresses are equal between the directions of pull. Second, the stresses on the unconstrained surface are negligible. Third, the hydrostatic pressure can be defined as the negative of the stresses in the unconstrained surface. Recall that these stresses are due to the effect of the deformation in the perpendicular directions.

$$\sigma_{11} = \sigma_{22} = \sigma^{*};$$

Equation 18

$$\sigma_{33} = 0;$$

Equation 19

$$p = -\sigma_{33};$$

Equation 20

Finally, these claims were used to derive the analytic solution for an incompressible, Mooney-Rivlin material undergoing biaxial tension.

$$\sigma^{*}_{MR} = \begin{bmatrix} 2c_1\left(\lambda^{*2} - \left(\frac{1}{\lambda^{*4}}\right)\right) + 2c_2\left(\lambda^{*4} - \left(\frac{1}{\lambda^{*2}}\right)\right) & 0 & 0 \\ 0 & 2c_1\left(\lambda^{*2} - \left(\frac{1}{\lambda^{*4}}\right)\right) + 2c_2\left(\lambda^{*4} - \left(\frac{1}{\lambda^{*2}}\right)\right) & 0 \\ 0 & 0 & 0 \end{bmatrix};$$

Equation 21

Fiber with exponential, power-law mechanics

The uncoupled strain energy function of the incompressible fibers, embedded within the structural model, was given by [11].

$$W_F(I_n) = \left(\frac{\xi}{\alpha\beta}\right)\left(\exp\left[\alpha(I_n - 1)^{\beta}\right] - 1\right);$$

Equation 22

Where $\xi > 0$, $\alpha \geq 0$, and $\beta \geq 2$. Moreover, in the limit when $\alpha \to 0$, the expression produces a power law formulation [11].

$$\lim_{\alpha \to 0} W_F(I_n) = \left(\frac{\xi}{\beta}\right)(I_n - 1)^{\beta};$$

Equation 23

When $\beta > 2$, the fiber modulus is zero at the origin. Hence, any value that follows this inequality ensures a smooth transition between compressive and tensile stresses [11]. Most importantly however, the term I_n represents the square of the fiber stretch λ_n^2 [11].

$$I_n = \lambda_n^2 = N \cdot C \cdot N;$$

Equation 24

The orientation of the fibers within each element of the structural model is given by the fiber-direction vector (N):

$$N = \sin(\varphi)\cos(\theta)\,\mathbf{e_1} + \sin(\varphi)\sin(\theta)\,\mathbf{e_2} + \cos(\varphi)\,\mathbf{e_3};$$

Equation 25

Where the angles follow the Cartesian system shown in (Figure #) [Appendix A]. Supposing a single fiber aligned in the principal direction of deformation, the Cauchy Stress tensor (σ) was derived from the strain energy function in Equation 22. The fibers must also be considered incompressible materials with isotropic behavior in the plane transverse to the principal deformation (Equation 6, Equation 7, and Equation 8). The

calculated stresses on the unconstrained surfaces was then used to calculate the hydrostatic pressure (Equation 10) and derive the final form of the Cauchy Stress tensor (σ).

$$\sigma_F^* = \begin{bmatrix} 2\xi\lambda^{*2}\exp\left(\alpha(\lambda^2-1)^\beta\right)(\lambda^{*2}-1)^{\beta-1} - 2\xi\left(\frac{1}{\lambda^*}\right)\exp\left(\alpha\left(\left(\frac{1}{\lambda^*}\right)-1\right)^\beta\right)\left(\left(\frac{1}{\lambda^*}\right)-1\right)^{\beta-1} & 0 & 0 \\ 0 & 0 & 0 \\ 0 & 0 & 0 \end{bmatrix};$$

Equation 26

Fibers, such as collagen in biological tissues, can only withstand tension [1, 15]. Hence, the model above only works when $\lambda^* > 1$. Therefore, the correct form of the fiber's strain energy density function and Cauchy Stress tensor (σ) must be multiplied by the Heaviside function [11].

$$W_F(I_n) = H(I_n - 1)\left(\frac{\xi}{\alpha\beta}\right)\left(\exp\left[\alpha(I_n-1)^\beta\right]-1\right);$$

Equation 27

$$\sigma_F^* = H(I_n - 1)\begin{bmatrix} 2\xi\lambda^{*2}\exp\left(\alpha(\lambda^2-1)^\beta\right)(\lambda^{*2}-1)^{\beta-1} - 2\xi\left(\frac{1}{\lambda^*}\right)\exp\left(\alpha\left(\left(\frac{1}{\lambda^*}\right)-1\right)^\beta\right)\left(\left(\frac{1}{\lambda^*}\right)-1\right)^{\beta-1} & 0 & 0 \\ 0 & 0 & 0 \\ 0 & 0 & 0 \end{bmatrix};$$

Equation 28

Continuous, two-dimensional (2D), Von-Mises distribution

Instead of embedding single fibers within the ground matrix of the structural model, continuous distributions have been used to better simulate the mechanical response of fibrous tissues [lanir, hump, ateshian, hozapfel].

Two-dimensional (2D), Von-Mises distributions are described by the function $R(n)$.

$$R(n) = \frac{\exp[b(2n_1^2 - 1)]}{2\pi I_0(b)};$$

Equation 29

In this function, n_1 represented the principal component of n, b the concentration parameter, and I_0 the Bessel function of the first kind of order 0 [11]. The behavior of the distribution was depicted in Figure # [Appendix – A]. The magnitude of $R(n)$ changes as a function of n, also a function of θ. Note that θ is analogous to that of the main coordinate system depicted in Figure # [Appendix – A].

$$n_1 = n\cos(\theta);$$

Equation 30

$$R(\theta) = \frac{\exp\left[b\left(2(n\cos\left(\theta\left(\frac{\pi}{180}\right)\right)^2) - 1\right)\right]}{2\pi I_0(b)};$$

Equation 31

These definitions were then coupled to the strain energy density function and Cauchy Stress tensor (σ) of the fibers, to complete the formulation of the mechanics of a fiber distribution.

$$W_F(I_n) = H(I_n - 1)\left(\frac{\xi}{\alpha\beta}\right)\left(\exp\left[\alpha(I_n - 1)^{\beta}\right] - 1\right)\int_{dA} R(n)dA\,;$$

Equation 32

$$\sigma_F^* = H(I_n - 1)\begin{bmatrix} 2\xi\lambda^{*2}\exp\left(\alpha(\lambda^2 - 1)^{\beta}\right)\left(\lambda^{*2} - 1\right)^{\beta-1} - 2\xi\left(\frac{1}{\lambda^*}\right)\exp\left(\alpha\left(\left(\frac{1}{\lambda^*}\right) - 1\right)^{\beta}\right)\left(\left(\frac{1}{\lambda^*}\right) - 1\right)^{\beta-1} & 0 & 0 \\ 0 & 0 & 0 \\ 0 & 0 & 0 \end{bmatrix}\int_{dA} R(n)dA\,;$$

Equation 33

Structural Model

The strain energy density function of the structural model was built from the addition of the constitutive formulations of each component, ground matrix and fibers.

$$W_{SM} = W_{MR}(I_1, I_2) + W_F(I_n);$$

Equation 34

Given that the stresses are proportional, the same additive property applies to the formulation of the Cauchy Stress tensor (σ) of the structural model.

$$\sigma^*_{SM} = \sigma^*_{MR} + \sigma^*_F;$$

Equation 35

Where the final form of the tensor varies on the basis of the experiment's kinematics.

Uniaxial

$$\sigma^*_{SM} = \begin{bmatrix} \left(2c_1 + \frac{2c_2}{\lambda^*}\right)\left(\lambda^{*2} - \frac{1}{\lambda^*}\right) & 0 & 0 \\ 0 & 0 & 0 \\ 0 & 0 & 0 \end{bmatrix} +$$

$$H(I_n - 1)\begin{bmatrix} 2\xi\lambda^{*2}\exp\left(\alpha(\lambda^2 - 1)^\beta\right)(\lambda^{*2} - 1)^{\beta-1} - 2\xi\left(\frac{1}{\lambda^*}\right)\exp\left(\alpha\left(\left(\frac{1}{\lambda^*}\right) - 1\right)^\beta\right)\left(\left(\frac{1}{\lambda^*}\right) - 1\right)^{\beta-1} & 0 & 0 \\ 0 & 0 & 0 \\ 0 & 0 & 0 \end{bmatrix}\int_{dA} R(n)dA;$$

Equation 36

Biaxial

$$\sigma^*_{SM} = \begin{bmatrix} 2c_1\left(\lambda^{*2} - \left(\frac{1}{\lambda^{*4}}\right)\right) + 2c_2\left(\lambda^{*4} - \left(\frac{1}{\lambda^{*2}}\right)\right) & 0 & 0 \\ 0 & 2c_1\left(\lambda^{*2} - \left(\frac{1}{\lambda^{*4}}\right)\right) + 2c_2\left(\lambda^{*4} - \left(\frac{1}{\lambda^{*2}}\right)\right) & 0 \\ 0 & 0 & 0 \end{bmatrix} +$$

$$H(I_n - 1)\begin{bmatrix} 2\xi\lambda^{*2}\exp\left(\alpha(\lambda^2 - 1)^\beta\right)(\lambda^{*2} - 1)^{\beta-1} - 2\xi\left(\frac{1}{\lambda^*}\right)\exp\left(\alpha\left(\left(\frac{1}{\lambda^*}\right) - 1\right)^\beta\right)\left(\left(\frac{1}{\lambda^*}\right) - 1\right)^{\beta-1} & 0 & 0 \\ 0 & 0 & 0 \\ 0 & 0 & 0 \end{bmatrix}\int_{dA} R(n)dA;$$

Equation 37

Appendix C – Tables and lists

Table 2: Dog bone or dumbbell dimensions		
Variable	Description	Units
l_o	Outer length	mm
l_i	Inner length	mm
l_g	Length of grip area	mm
w_o	Outer width	mm
w_i	Inner width	mm
R	Radius of curvature	mm

Table 3: Dog bone geometric relations		
Variable	Equivalence	Description
α	l_i/l_o	Length ratio (inner/outer)
β	w_i/w_o	Width ratio (inner/outer)
l_g	$3(l_O - l_i)/8$	Length of grip area
R	$(w_o - w_i)/2$	Radius of curvature

Table 4: Dog bone geometric variants							
α	*β*	*lo (mm)*	*li (mm)*	*lg (mm)*	*Wo (mm)*	*Wi (mm)*	*R (mm)*
0.1250	0.6250*	10.0000	1.2500	3.2813	3.0000	1.8750	0.5625
0.1250	0.7500	10.0000	1.2500	3.2813	3.0000	2.2500	0.3750
0.1250	0.8750	10.0000	1.2500	3.2813	3.0000	2.6250	0.1875
0.2500	0.2500*[2]	10.0000	2.5000	2.8125	3.0000	0.7500	1.1250
0.2500	0.3750	10.0000	2.5000	2.8125	3.0000	1.1250	0.9375
0.2500	0.5000	10.0000	2.5000	2.8125	3.0000	1.5000	0.7500
0.2500	0.6250	10.0000	2.5000	2.8125	3.0000	1.8750	0.5625
0.2500	0.7500	10.0000	2.5000	2.8125	3.0000	2.2500	0.3750
0.2500	0.8750	10.0000	2.5000	2.8125	3.0000	2.6250	0.1875
0.3750	0.1250	10.0000	3.7500	2.3438	3.0000	0.3750	1.3125
0.3750	0.2500	10.0000	3.7500	2.3438	3.0000	0.7500	1.1250
0.3750	0.3750	10.0000	3.7500	2.3438	3.0000	1.1250	0.9375
0.3750	0.5000	10.0000	3.7500	2.3438	3.0000	1.5000	0.7500
0.3750	0.6250	10.0000	3.7500	2.3438	3.0000	1.8750	0.5625
0.3750	0.7500	10.0000	3.7500	2.3438	3.0000	2.2500	0.3750
0.3750	0.8750	10.0000	3.7500	2.3438	3.0000	2.6250	0.1875
0.5000	0.1250	10.0000	5.0000	1.8750	3.0000	0.3750	1.3125

0.5000	0.2500	10.0000	5.0000	1.8750	3.0000	0.7500	1.1250
0.5000	0.3750	10.0000	5.0000	1.8750	3.0000	1.1250	0.9375
0.5000	0.5000	10.0000	5.0000	1.8750	3.0000	1.5000	0.7500
0.5000	0.6250	10.0000	5.0000	1.8750	3.0000	1.8750	0.5625
0.5000	0.7500	10.0000	5.0000	1.8750	3.0000	2.2500	0.3750
0.5000	0.8750	10.0000	5.0000	1.8750	3.0000	2.6250	0.1875
0.6250	0.1250	10.0000	6.2500	1.4063	3.0000	0.3750	1.3125
0.6250	0.2500	10.0000	6.2500	1.4063	3.0000	0.7500	1.1250
0.6250	0.3750	10.0000	6.2500	1.4063	3.0000	1.1250	0.9375
0.6250	0.5000	10.0000	6.2500	1.4063	3.0000	1.5000	0.7500
0.6250	0.6250	10.0000	6.2500	1.4063	3.0000	1.8750	0.5625
0.6250	0.7500	10.0000	6.2500	1.4063	3.0000	2.2500	0.3750
0.6250	0.8750	10.0000	6.2500	1.4063	3.0000	2.6250	0.1875
0.7500	0.1250	10.0000	7.5000	0.9375	3.0000	0.3750	1.3125
0.7500	0.2500	10.0000	7.5000	0.9375	3.0000	0.7500	1.1250
0.7500	0.3750	10.0000	7.5000	0.9375	3.0000	1.1250	0.9375
0.7500	0.5000	10.0000	7.5000	0.9375	3.0000	1.5000	0.7500
0.7500	0.6250	10.0000	7.5000	0.9375	3.0000	1.8750	0.5625
0.7500	0.7500	10.0000	7.5000	0.9375	3.0000	2.2500	0.3750
0.7500	0.8750	10.0000	7.5000	0.9375	3.0000	2.6250	0.1875
0.8750	0.1250	10.0000	8.7500	0.4688	3.0000	0.3750	1.3125
0.8750	0.2500	10.0000	8.7500	0.4688	3.0000	0.7500	1.1250
0.8750	0.3750	10.0000	8.7500	0.4688	3.0000	1.1250	0.9375
0.8750	0.5000	10.0000	8.7500	0.4688	3.0000	1.5000	0.7500
0.8750	0.6250	10.0000	8.7500	0.4688	3.0000	1.8750	0.5625
0.8750	0.7500	10.0000	8.7500	0.4688	3.0000	2.2500	0.3750
0.8750	0.8750	10.0000	8.7500	0.4688	3.0000	2.6250	0.1875

*, *[2] Ratios were not normalized or constrained to the total length of the geometry. Therefore, some variants could not be drawn.

Table 5: Cruciform dimensions		
Variable	Description	Units
w_o	Outer width	mm
w_i	Inner width	mm
w_a	Width of cruciform arm	mm
R	Radius of curvature	mm

Table 6: Cruciform geometric relations		
Variable	Equivalence	Description
w_i	$2w_o/5$	Inner width
w_a	$3w_o/10$	Width of cruciform arm
R	γw_a*	Radius of curvature

* The ratio γ varies to generate a range of curvatures and, thus, a range of geometric variants

Table 7: Cruciform geometric variants				
γ	*Wo (mm)*	*Wi (mm)*	*Wa (mm)*	*R (mm)*
0.0000	10	4	3	0.0000
0.0625	10	4	3	0.1875
0.1250	10	4	3	0.3750
0.1875	10	4	3	0.5625
0.2500	10	4	3	0.7500
0.3125	10	4	3	0.9375
0.3750	10	4	3	1.1250
0.4375	10	4	3	1.3125
0.5000	10	4	3	1.5000
0.5625	10	4	3	1.6875
0.6250	10	4	3	1.8750
0.6875	10	4	3	2.0625
0.7500	10	4	3	2.2500
0.8125	10	4	3	2.4375
0.8750	10	4	3	2.6250
0.9375	10	4	3	2.8125
1.0000	10	4	3	3.0000

Table 8: Validation of ground matrix			
Variable	Description	Value	Units
Material Model: Mooney Rivlin			
C1	Model coefficient	1	Pa
C2	Model coefficient	0.1	Pa
K*	Bulk Modulus	1000	Pa
Tensile Deformation Parameters			
l	Input Displacement	1	mm
dl/dt	Displacement/Strain Rate	1	mm/sec.
FEBio Simulation Parameters			
K*	Penalty Factor	1000	Pa
ε	Lagrangian Tolerance	1	%

* In the case of the Mooney-Rivlin model, the penalty factor represents the bulk modulus (K) of the material. In other words, the penalty factor has a physical meaning to the model.

Table 9: Uniaxial, tensile experiment for dog bone variants			
Variable	Description	Value	Units
FEBio Simulation Parameters*	Final Displacement*[2]	10[1, 0, 0]*[3]	mm
	Final Time*[3]	10	sec.
	Displacement Rate	1	mm/sec.
	Time steps	125	Steps*sec.
	Step size	0.01	1/Steps
	Max step	0.01	Steps
t_{sim}*[4]	Simulation Time	1.25	sec.

* The tensile experiments have been described using FEBio terminology and parameters. Hence, no variables exist for the majority of these parameters.

*2 In FEBio, the displacement stimulus was described with a load curve (load vs. time). Given that the simulation started at rest, the initial displacement was zero (0 mm) and only the final displacement was reported. In the same manner, the initial time was zero (0 sec.) and the only the final time was reported.

*3 Uniaxial tests consisted of a controlled displacement along X(1). Therefore, the final displacement was reported as magnitude and direction vector.

*4 In FEBio, the duration of the simulation was determined, indirectly, through the product between the variables “Time steps” and “Step size.”

Table 10: Biaxial, tensile experiment for dog bone variants			
Variable	Description	Value	Units
FEBio Simulation Parameters*	Final Displacement*[2]	10[1, 1, 0]*[3]	mm
	Final Time*[3]	10	sec.
	Displacement Rate	1	mm/sec.
	Time steps	125	Steps*sec.
	Step size	0.01	1/Steps
	Max step	0.01	Steps
t_{sim}*[4]	Simulation Time	1.25	sec.

* The tensile experiments have been described using FEBio terminology and parameters. Hence, no variables exist for the majority of these parameters.

*2 In FEBio, the displacement stimulus was described with a load curve (load vs. time). Given that the simulation started at rest, the initial displacement was zero (0 mm) and only the final displacement was reported. In the same manner, the initial time was zero (0 sec.) and the only the final time was reported.

*3 Biaxial tests consisted of a controlled displacement along $X(1)$ and $Y(2)$. Therefore, the final displacement was reported as magnitude and direction vector.

*4 In FEBio, the duration of the simulation was determined, indirectly, through the product between the variables "Time steps" and "Step size."

Table 11: Regions of interest (ROIs)		
Name	Variable	Description
Target	σ_t	Volumetric region where concentrations are desired
Intensities	σ_{si}	Volumetric region where concentrations are undesired
Maximum	σ_m	Volumetric region center at the maximum value measured on the mesh
Boundaries	σ_{bc}	Volumetric region corresponding to the gripping boundaries*